

# **Development of evolution drugs - antibacterial compounds that block pathways to resistance.**

Yanmin Zhang<sup>1,2#</sup>, Sourav Chowdhury<sup>2#</sup>, João V. Rodrigues<sup>2</sup>, Eugene. Shakhnovich<sup>2</sup>

<sup>1</sup>School of Science, China Pharmaceutical University

639 Longmian Avenue, Jiangning District

Nanjing, Jiangsu 211198

P.R China

<sup>2</sup>Department of Chemistry and Chemical Biology

Harvard University

12 Oxford Street Cambridge MA 02138

# contributed equally

## Abstract

Antibiotic resistance is a worldwide challenge. A potential approach to block resistance is to simultaneously inhibit WT and known escape variants of the target bacterial protein. Here we applied an integrated computational and experimental approach to discover compounds that inhibit both WT and trimethoprim (TMP) resistant mutants of *E. coli* dihydrofolate reductase (DHFR). We identified a novel compound (CD15-3) that inhibits WT DHFR and its TMP resistant variants L28R, P21L and A26T with  $IC_{50}$  50-75  $\mu$ M against WT and TMP-resistant strains. Resistance to CD15-3 was dramatically delayed compared to TMP in *in vitro* evolution. Whole genome sequencing of CD15-3 resistant strains showed no mutations in the target *folA* locus. Rather, gene duplication of several efflux pumps gave rise to weak (about twofold increase in  $IC_{50}$ ) resistance against CD15-3. Altogether, our results demonstrate the promise of strategy to develop evolution drugs - compounds which block evolutionary escape routes in pathogens.

## 1. Introduction

Fast paced artificial selection in bacteria against common antibiotics has led to the emergence of highly resistant bacterial strains which potentially render a wide variety of antibiotics clinically ineffective. Emergence of these “superbugs” including ESKAPE (*Enterococcus faecium*, *Staphylococcus aureus*, *Klebsiella pneumoniae*, *Acinetobacter baumannii*, *Pseudomonas aeruginosa*, and *Enterobacter spp.*) (Peneş et al., 2017) call for novel approaches to design antibiotic compounds that act as “evolution drugs” by blocking evolutionary escape from antibiotic stressor.

Selectively targeting bacterial proteins which are critical to essential bacterial life processes like cell wall biosynthesis, translation, DNA replication etc. with novel compounds forms the basis of antibiotics development programs. Dihydrofolate reductase (DHFR) is one such protein, which, due to its critical role in nucleotide biosynthesis, has been a central drug target (Lin and Bertino, 1991; Schweitzer et al., 1990). Based on the chemical scaffold, DHFR inhibitors can be divided into classical and non-classical ones. The classical DHFR inhibitors generally contain a 2,4-diamino-1,3-diazapharmacophore group (Bharath et al., 2017) which constitute structural analogues of its substrate dihydrofolate and competitively bind the receptor-DHFR active site. Inhibitors of this type such as methotrexate (MTX) (Bleyer, 2015) and pralatrexate (PDX) (Izbicka et al., 2009) are approved as anticancer drugs. In addition, predominant classes of inhibitors derived from dihydrofolate analogues also include diaminoquinazoline, diaminopyrimidine, diaminopteridine, and diaminotriazines (Bharath et al., 2017). Non-classical antifolate drugs like trimethoprim (TMP) (Finland and Kass, 1973) trimetotrexate (TMQ) (Lin and Bertino, 1991), that interact selectively with bacterial but not human DHFR are approved as antibacterial drugs. Without the solvent accessible group of glutamic acid, they are more fat-soluble, passively diffuse into cells, and are also not substrates for folylpolyglutamate synthetase enzymes. However, due to rapid emergence of resistant mutations in DHFR, the development of drug resistance to antifolate antibiotics belonging to any of the above-mentioned classes presents a significant challenge (Huovinen et al., 1995). Both clinical and in vitro studies have shown that accumulation of point mutations in critical amino acids residues of the binding cavity represent an important mode of trimethoprim resistance.

Mutations conferring resistance in bacteria to anti-DHFR compounds are primarily located in the *folA* locus that encodes DHFR in *E. coli* (Oz et al., 2014; Tamer et al., 2019; Toprak et al., 2012) making DHFR an appealing target to develop evolution antibiotic drugs. A possible approach is to design compounds that can inhibit the wild type (WT) DHFR along with its resistant variants thus blocking multiple evolutionary pathways towards drug-resistance. In this work, we developed an integrative computational modeling and biological evaluation workflow to discover novel DHFR inhibitors that are active against WT and resistant variants. Structure-based virtual screening (SBVS) including molecular docking with subsequent molecular dynamics (MD)

(Cheron and Shakhnovich, 2017; Leonardo et al., 2015; Liu et al., 2020; Zhang et al., 2018) validation were used to screen a large compound database. A series of DHFR inhibitors with novel scaffolds that are active against both the WT and several mutant DHFR proteins and are cytotoxic against WT *E. coli* along with *E. coli* strains with chromosomally incorporated TMP resistant DHFR variants (Palmer et al., 2015). Those inhibitors are more potent against the escape variants than the WT DHFR. This makes them promising candidates for further development of next generation of antibiotics that prevent fast emergence of resistance. Together, these results represent a comprehensive multiscale and multitool approach to address antibiotic resistance.

## Results

### *In silico search for potent broad DHFR inhibitors.*

The key objective of our approach is to find compounds that *simultaneously* inhibit WT and drug resistant variants of a target protein. Firstly, we developed an integrative computational workflow including molecular docking, molecular dynamics and evaluation of protein-ligand interaction along with Lipinski's rule of five (Manto et al., 2018) filter to screen two commercial databases that include about 1.8 million compounds (Figure 1A). First, we assessed which conformation of M20 loop of DHFR (closed, open or occluded) should be used for molecular docking. To that end we evaluated which conformation of the M20 loop in the target structure gives rise to best agreement between docking score and experimental binding affinity for known DHFR inhibitors. By classification (see Supplementary Information. *Crystal structure selection*), we selected four representative crystal structures (closed: PDB 1RX3, open: PDB 1RA3, occluded: PDB 1RC4 and PDB 5CCC, Figure S1) as putative target structures for docking. Using the closed conformation of M20 loop (PDB 1RX3), we were able to recover the largest proportion of known inhibitors (Table S1 and Figure S2-S3). Therefore, the closed conformation of M20 loop (PDB 1RX3) was adopted as the most representative crystal structure for the initial SBVS of compound databases for novel broad range inhibitors. It was also used for subsequent in-depth evaluation of most promising candidates using molecular dynamics simulation. The detailed discussion of the rationale behind selection of closed conformation is provided in the Supplementary Information (*Crystal structure selection*).

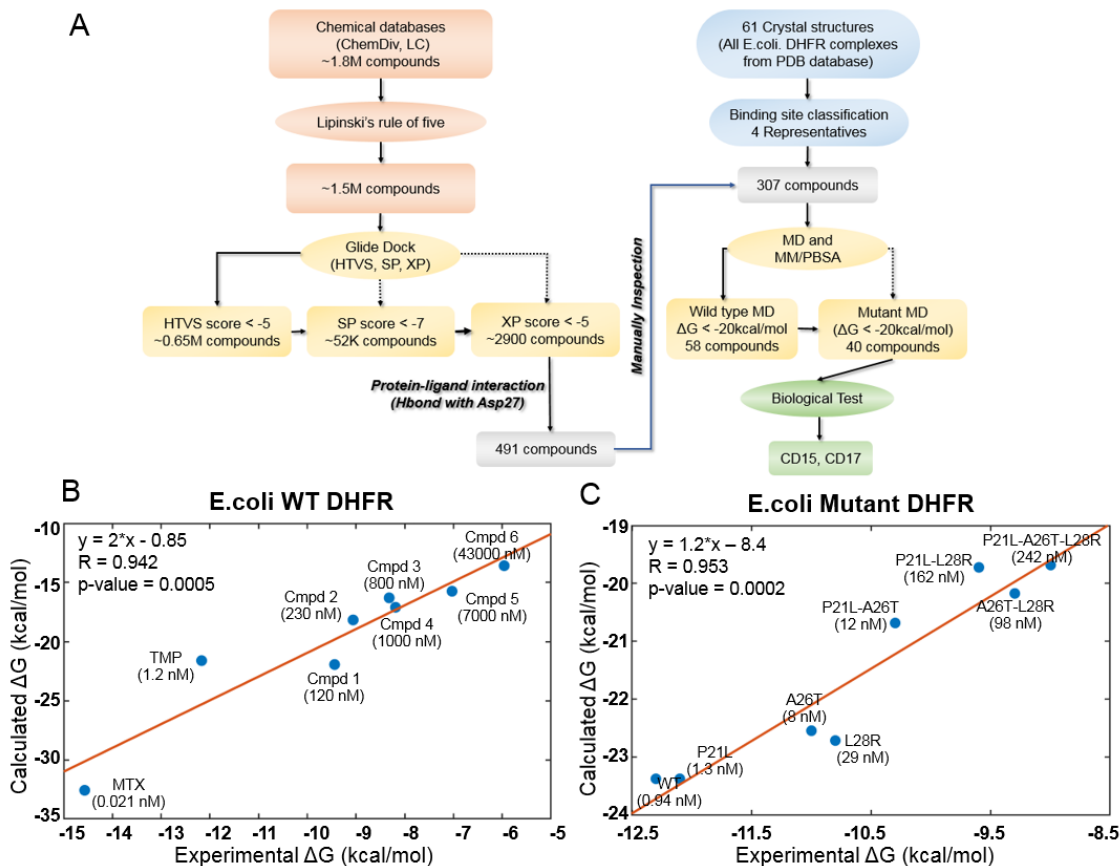


**Figure 1 - Computational design of broadly neutralizing DHFR inhibitors effective against WT and resistant DHFR mutant strains.** *A*) Integrative virtual screening workflow. Detailed description of the virtual screening workflow can be found in *Supplementary Information (Selection of virtual screening hits)* *B*) Linear model for binding affinity prediction constructed using known binding affinities of eight known inhibitors of WT *E. coli* DHFR (Figure S4) obtained from (Carroll et al., 2012). *C*) Linear model for binding affinity prediction constructed using experimental inhibitory activity for TMP against WT DHFR and seven resistant DHFR mutants (Rodrigues et al., 2016). MD simulation and MM/PBSA affinity evaluation protocol (Cheron and Shakhnovich, 2017) was applied to calculated binding free energy of complexes of *E. coli* DHFR with eight known inhibitors and the calculated values were compared with the reported experimental binding affinities ( $K_d$  or  $K_i$  values).

A total of 307 candidate compounds with strongest docking score that form hydrogen bond with the critical residue Asp27 in the DHFR binding pocket, were submitted for more accurate prediction of binding free energy (Cheron and Shakhnovich, 2017) (Figure 1A). Our approach to predict binding free energy is based on a series of relatively short MD simulations of binding conformations with subsequent MMPBSA scoring as presented in (Cheron and Shakhnovich, 2017). Next, we assessed the accuracy of this approach for WT and mutant DHFR in reproducing binding affinities of known ligands. To that end we built linear regression equation models (see Figure 1B and Figure 1C and Supporting Information. *Binding Affinity Prediction Model*) to predict binding free energies calculated by MMPBSA.

The models reproduced known binding affinities with high accuracy (see Figure 1 B,C and Figures S4 and S6). Additionally, we constructed linear regression equation models to predict binding free energy of TMP against WT and mutant DHFR from *Listeria grayi* (*L. grayi*) and *Chlamydia muridarum* (*C. muridarum*) again showing highly significant correlation between predicted and experimental values (Figure S7), demonstrating broad predictive power of the method. More detail on the construction of binding affinity prediction models can be found in the Supplementary Information (*Model to Predict Binding Affinity*).

Further, the analysis of the DHFR crystal structures showed that Asp27 forms hydrogen bond with almost all DHFR inhibitors in the ligand binding cavity. Thus, compounds predicted by docking that make hydrogen bond with Asp27 (Figure 1A) and having MMPBSA predicted binding free energies less than -20 kcal/mol (See Supplementary Materials. *Compound Information*) against both the WT and all TMP-resistant variants of DHFR were selected for further evaluation. Out of this set, we selected the novel compounds that differ substantially from 183 known DHFR inhibitors (see Supplementary Information. Selection of Virtual Screening Hits)). Generally, compounds with similar properties tend to have similar activity (Kumar, 2011). Based on that principle, we compared two-dimensional (2D) physicochemical properties (Zhang et al., 2013) and protein-ligand interaction fingerprint (PLIF) features (Marcou and Rognan, 2007) of the prospective set with those of the known inhibitors. Results showed that the selected hits have high similarity in both 2D-physicochemical properties and PLIF features when compared with known DHFR inhibitors, which suggest their potential inhibitory activity against DHFR (Figure S8-S9). On the other hand, they show relatively low chemical similarity (Figure S8) with the known DHFR inhibitors, suggesting that the selected hits are chemically novel. Altogether, a total of 40 prospective active compounds were purchased for evaluation. The detailed information on all compounds can be found in Supplementary Materials (*Compound Information*). Further details on SBVS can be found in the Supplementary Information (*Selection of Virtual Screening Hits*).

#### *Assaying prospective compounds in vitro*

Spectrophotometry assay (Rodrigues et al., 2016) (See Materials and Methods) was employed to evaluate possible inhibition of catalytic activity of the 40 selected compounds against WT DHFR and its TMP resistant mutants including P21L, A26T and L28R (Figure 2). The drop in fluorescence upon conversion of NADPH to NADP<sup>+</sup> for the reaction system reported on inhibition of DHFR catalytic activity. All 40 prospective compounds were initially assayed for inhibition of DHFR at a single fixed concentration of 200  $\mu$ M. As shown in Figure 2A-2B and Figure S10, a total of 13, 8, 6 and 14 compounds resulted in more than 20% loss of the DHFR catalytic activity at that concentration for WT, P21L, A26T and L28R DHFR, respectively. Among them, compounds CD15, CD17 and CD08 showed more than 30% inhibition against both WT and all three DHFR mutants (Figure 2C and Figure S10). Compound CD20, with similar scaffold to that of TMP, showed inhibition against WT, P21L and A26T, but not L28R DHFR and was no longer considered. Thus, a total of three hits including compounds CD15, CD17 and CD08 (Figure 2C) were further evaluated for concentration-dependent inhibition of all DHFR variants

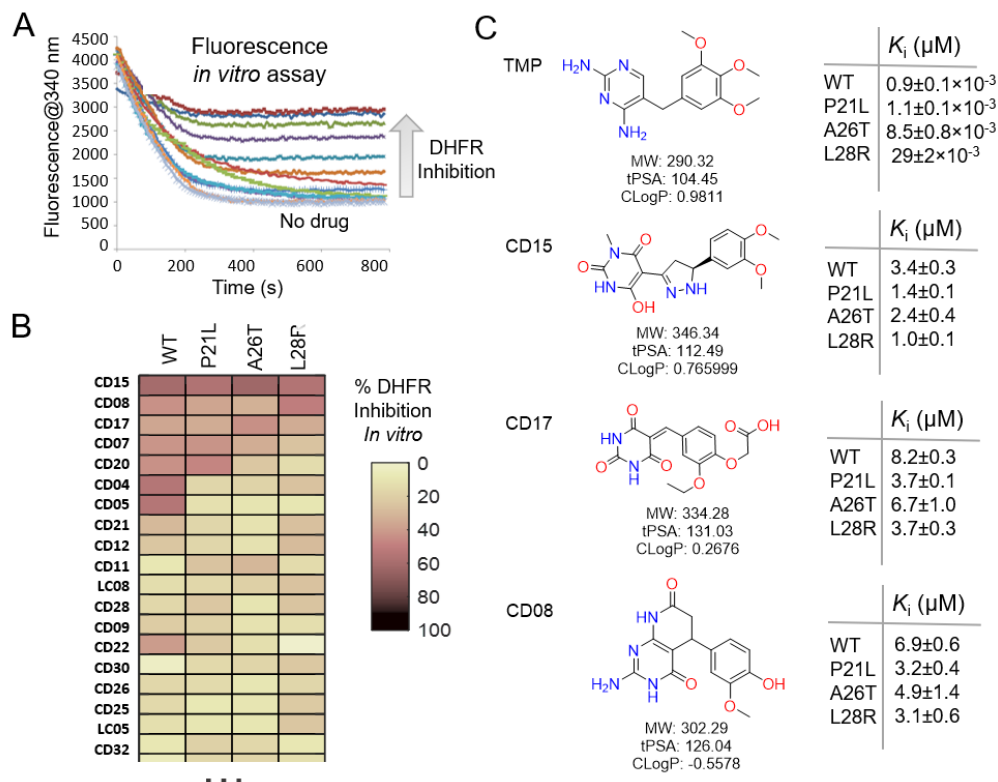


**Figure 2–Evaluation of the potential hits *in vitro* and their optimization.** A-B) An *in vitro* kinetic assay of DHFR catalytic activity was used to screen inhibitors against WT DHFR and three single mutants resistant to TMP (P21L, A26T and L28R). C) Chemical structures of the top three compounds showing simultaneously the highest potency against WT and mutant DHFR variants. The structure of trimethoprim is shown for comparison.

Two of the three compounds, CD15 and CD17 with two novel scaffolds, inhibited WT and mutant DHFRs in concentration-dependent manner (Figure 3). We used inhibition curves (Figure 3), to obtain  $IC_{50}$  values and converted them into corresponding  $K_i$  values (Table S2). For compound CD15, the  $K_i$  values were all less than  $5\mu\text{M}$  against WT and three single-point DHFR mutants. For the L28R mutant the  $K_i$  values were  $1.04\mu\text{M}$ , outperforming the WT, P21L or A26T mutant DHFR. It is worth noting that L28R is a strong TMP escape variant (Rodrigues et al., 2016; Toprak et al., 2012), thus the discovered CD15 series appeared a promising candidate for an “evolution drug” that has a potential to suppress even most intractable escape variants. Based on these data we decided to proceed with compounds CD15 and CD17 for in depth evaluation. In addition, we evaluated the inhibition of catalytic activity of the two most promising inhibitors, CD15 and CD17 against WT DHFR from two more species: *L.grayi* and *C.muridarum*. We found that both compounds showed similar inhibitory activity against the two species (See Figure 3 and Table S2). These results suggest that those two compounds could be used as broadly efficient potential antibacterial leads.

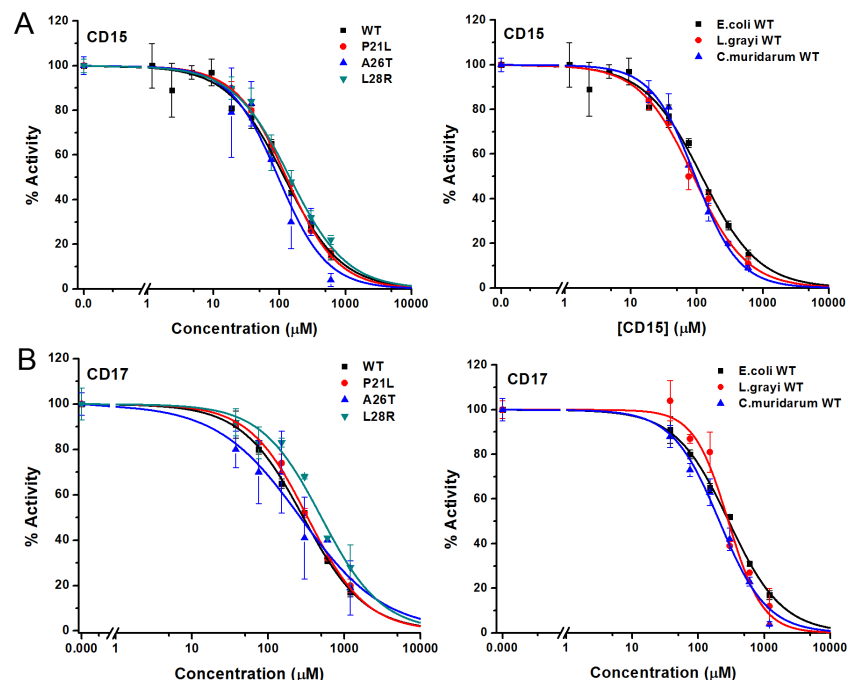


**Figure 3— The concentration-dependent inhibition of WT and mutant DHFR from different species by compounds CD15 and CD17. A) Concentration-dependent inhibition curves for compound CD15 for WT and mutant DHFR of *E.coli* (left panel) and for WT and mutant DHFR from *L.grayi*, and *C.muridarum*, respectively (right panel). B) Concentration-dependent inhibition curves for compound CD17 on WT and mutant DHFR of *E.coli* (left panel) and of WT and mutant DHFR from *L. grayi*, and *C. muridarum*, respectively (right panel). The %Activity of the y-axis is represented by the decrease of fluorescence at 340nm for the reaction system (see Methods for more detail)**

We also evaluated inhibitory activity of CD15 against double resistant mutants and found that they are approximately as active or better than against single mutants (see Table S2)

#### *Broad antimicrobial activity of new compounds*

Since two of the 40 compounds inhibit both WT and mutant proteins in vitro, we proceeded to test their efficacy to inhibit growth of *E. coli*. Previously (Rodrigues et al., 2016) we used strains with chromosomal replacement of WT *folA* with *folA* gene encoding three single mutants including P21L, A26T and L28R (Palmer et al., 2015). All mutant *E. coli* strains with the chromosomal *folA* replaced by three drug-resistant variants including P21L, A26T and L28R exhibit elevated resistance to TMP (Rodrigues et al., 2016). In particular, IC<sub>50</sub> of TMP for *E. coli* strain with chromosomal L28R DHFR is about 50 times higher than of WT strain (Palmer et al., 2015; Rodrigues et al., 2016). As shown in Figure 4A and 4B, dose-response curves clearly demonstrated that both CD15 and CD17 inhibit growth of the WT and three single *folA* mutant *E. coli* strains. The IC<sub>50</sub> values of CD15 and CD17 can be found in Table 1. Importantly, in terms of IC<sub>50</sub> CD15 outperformed TMP about 4-fold on the most resistant variant L28R. These results are consistent with the in vitro enzymatic activity assays (Figure 2C) showing that both CD15



and CD17 inhibited DHFR activity of L28R variant stronger than WT, accordingly these compounds inhibited growth of the L28R variant stronger than the WT and the other two mutants.

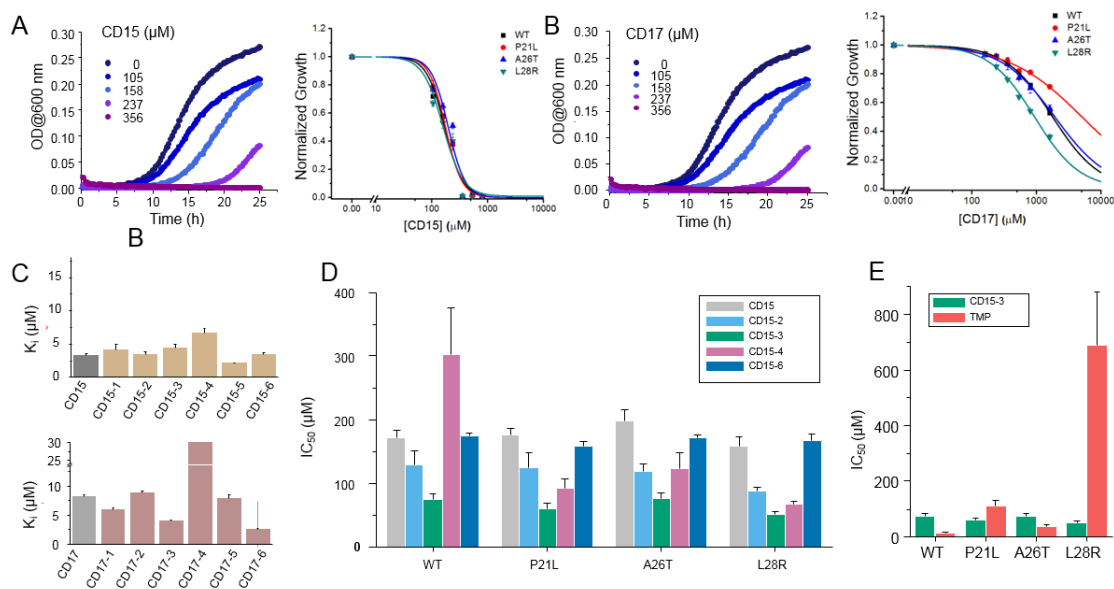


**Figure 4. Compounds CD15 and CD17 inhibit growth of WT and TMP-resistant mutant *E. coli* strains.** *A)* Growth curves for WT strain (left panel) at different concentrations of CD15 and normalized (by maximal growth in the absence of stressor) inhibition by CD15 curves for WT and various TMP resistant DHFR mutants. *B)* same as *A* for CD17. Measurements in the presence of different drug concentrations were performed in a 96-well microplate at 37°C. *C)* Optimization of compounds CD15 (upper panel) and CD17 (lower panel) lead to hits with increased in vitro inhibitory potency towards WT *E. coli* DHFR. *D)* The CD15 series compounds inhibit growth of WT and resistant mutant *E. coli* strains. For each strain, growth measurements were performed in the presence of varying concentrations of compounds. *E)* Comparison of  $IC_{50}$  of inhibition of growth of WT and TMP-resistant mutant *E. coli* strains for CD15-3 and TMP.

#### Compound optimization

While both CD15 and CD17 showed desired biological activity their  $IC_{50}$  for growth inhibition were relatively weak, so we proceeded to optimize both compounds to improve their efficacy. To that end, we searched the ChemDiv database (<http://www.chemdiv.com/>) for compounds that are similar to CD15 and CD17. The search yielded a total of 12 extra compounds which were subsequently obtained and evaluated for their inhibitory activity against DHFR *in vitro* and as inhibitors of *E. coli* bacterial growth. The inhibitory  $K_i$  values against WT DHFR were in the range of 2.22  $\mu\text{M}$  to 7.86  $\mu\text{M}$  for the 6 compounds from the CD15 series and in the range of 2.57  $\mu\text{M}$  to 27.83  $\mu\text{M}$  for the 6 compounds from the CD17 series (Figure 4C). Four compounds including CD15-2, CD15-3, CD15-4 and CD15-6 showed better or comparable inhibition for WT and L28R DHFR than CD15 (Figure 4C). Next, we evaluated in vivo activity of these compounds. Results showed that the compound CD15-3 with a naphthalene group (Figure 5A) instead of the trimethoxybenzene of CD15 (Figure 2C) showed marked improvement of efficacy

with 3- to 4 times lower IC<sub>50</sub> values compared to that of CD15 (Figure 4D). Particularly, CD15-3 showed about 18-fold better efficacy than that of TMP on L28R *E. coli* variant strain (Figure 4E). Improved topological polar surface area (tPSA) and clogP of CD15-3 is likely to be responsible for its superior efficacy of the bacterial growth inhibition on WT and mutant strains than other CD15 series compounds (Figure 5A). The IC<sub>50</sub> values of growth inhibition activity are listed in Table 1. Most of the CD17 series compounds did not show significantly better efficacy against L28R than the original CD17 (see Table 1). To address a possibility that CD17 series is a “false positive” targeting another protein(s) we turned to pan assay interference compounds (PAINS) filter that seeks compounds which tend to react non-specifically with numerous biological targets simultaneously rather than specifically affecting one desired target (Baell and Holloway, 2010). Thus, all 12 CD15 and CD17 series compounds were filtered through the PAINS (<http://cbligand.org/PAINS/>) (Baell and Holloway, 2010). All six CD17 series compounds did not pass the PAINS test and therefore were not considered for further analysis.

Table 1 The IC<sub>50</sub> values for the in vivo inhibition of several CD15 and CD17 series compounds

DHFR	Bacterial growth inhibition IC <sub>50</sub> (μM)										
	CD15	STD <sup>a</sup>	CD15-2	STD	CD15-3	STD	CD15-4	STD	CD15-6	STD	TMP
WT	170.97	12.12	129.04	21.68	<b>57.14</b>	6.46	302.37	73.53	174.50	4.05	13
P21L	176.24	10.12	124.88	23.52	<b>45.57</b>	6.78	92.25	15.37	158.87	6.26	111
A26T	197.24	18.20	118.94	10.81	<b>58.18</b>	6.12	122.52	24.94	172.14	4.38	38
L28R	159	14.63	87.72	6.46	<b>38.67</b>	4.61	67.10	4.22	166.95	10.18	691

DHFR	Bacterial growth inhibition IC <sub>50</sub> (μM)					
	CD17	STD	CD17-3	STD	CD17-4	STD
WT	1774.27	22.22	2945.81	966.63	ND <sup>b</sup>	ND
P21L	5048.24	809.68	2845.06	436.83	ND	ND
A26T	1920.51	135.16	2151.64	265.43	ND	ND
L28R	932.82	44.32	907.11	56.59	1856.89	271.63

<sup>a</sup>STD means the standard error from three duplicate experiments.

<sup>b</sup>ND (not determined) indicates no result was obtained for the compound against WT and three mutant DHFR.

The binding mode of the two most promising compounds CD15 and CD15-3 were evaluated using molecular docking (Figure 1a, Glide XP mode) with the target *E. coli* DHFR (PDB 1RX3). As shown in Figure 5B and 5C, both compounds formed two hydrogen bonds with the key residue Asp27 by the hydroxy group in the 6-hydroxy-3-methylpyrimidine-2,4(1H,3H)-dione scaffold. The binding modes of CD15 and CD15-3 overlapped perfectly with the binding conformation of TMP, providing rationale for the inhibitory activity of CD15 series. However, in addition to the hydrogen bond formed with Asp27, TMP also forms hydrogen bond with another critical residue Ile94 as well as the conserved water molecule HOH302. Nevertheless, unlike TMP, our hit compounds showed broad inhibitory activity in vitro and in vivo on both the WT and mutant DHFR strains. The broad activity of CD15 compounds can be explained, in part by a dihydro-1H-pyrazole group in the same position as methylene group of TMP. Naphthalene group of CD15-3 extends further in DHFR binding pocket than the corresponding trimethoxybenzene

of TMP, potentially resulting in additional hydrophobic interaction with L28R in DHFR which provides structural rationale for strong potency of CD15-3 against resistant L28R variant.

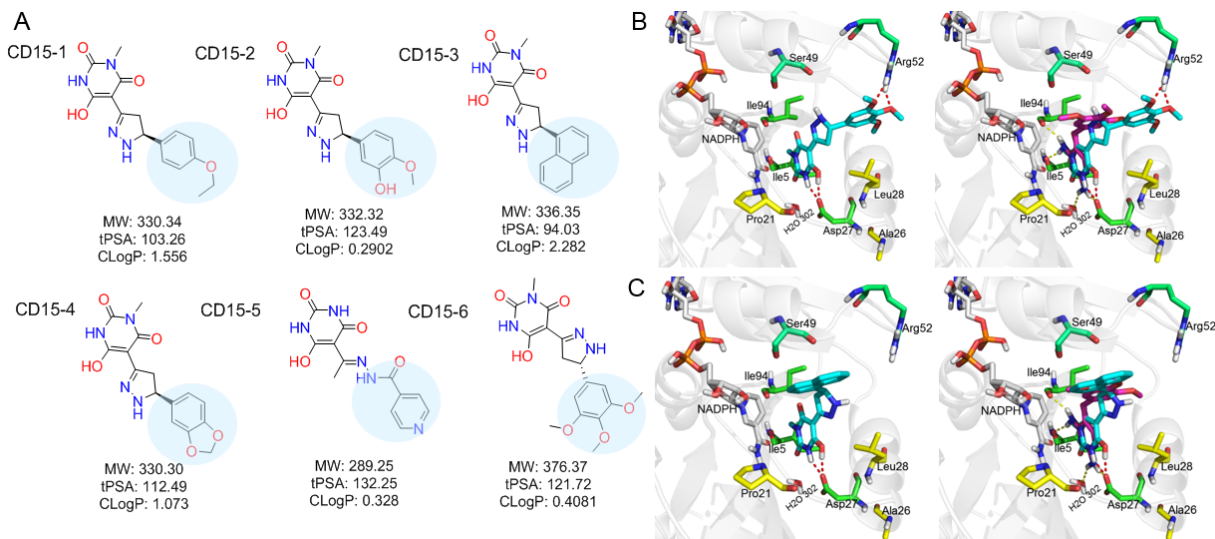


**Figure 5 Optimization of the compounds of CD15 series** A) Chemical structures of 2<sup>nd</sup> generation variants of compound CD15 selected for further experimental testing. B) The binding interaction of CD15 with DHFR (left panel) and the alignment of CD15 (cyan stick) with TMP (purple stick) in the binding pocket (right panel). C) The binding interaction of CD15-3 with DHFR (left panel) and the alignment of CD15-3 (cyan stick) with TMP (purple stick) in the binding pocket (right panel).

#### Target validation in vivo.

To confirm DHFR as the intracellular target of CD15-3 we overexpressed DHFR to assess whether it rescues growth inhibition by CD15-3. To that end we transformed *E. coli* BW27783 cells with pBAD plasmid (empty plasmid for the control and with *folA* gene for DHFR expression). BW27783 cells constitutively express arabinose transporters providing rather homogeneous response from the cell pool under arabinose induction (Bhattacharyya et al., 2016). Interestingly controlled expression of *folA* (encoding DHFR) under pBAD promoter with 0.005% arabinose induction partially rescued growth in a certain range of CD15-3 concentrations (Figure.6A). This improvement of growth rate was less pronounced at higher concentration of CD15-3. For control we used WT cells transformed with empty pBAD plasmids (without *folA* gene) and observed no effect on growth.

To further probe whether CD15-3 inhibits intracellular DHFR we overexpressed an inactive variant of DHFR, D27F mutant using the same pBAD-promoter where the expression was induced by 0.005% external arabinose (Rodrigues and Shakhnovich, 2019; Tian et al., 2015). In our experiment when D27F mutant form of DHFR was overexpressed we did not observe any growth rescue in cells treated with CD15-3. Growth rate profiles (Figure 6B) were almost identical, and no rescue of growth rate was observed in any of the concentration regimes of CD15-3 in this case. This result showed that inhibition of DHFR was, at least partially,

responsible for inhibition of cellular growth induced by CD15-3. As TMP is a known inhibitor of DHFR (WT) we wanted to check if these overexpression plasmid systems behave in a similar way as in the case of CD15-3 inhibition. Similar trend was observed for cells treated with TMP. Overexpression of WT DHFR recovered growth rate in TMP treated cells (Figure S11). No growth rescue from TMP induced inhibition was observed upon overexpression of D27F mutant (Figure S11).

These results indicate that DHFR is an intracellular target for the new compound CD15-3. However, a possibility remains that CD15-3 does not target DHFR exclusively. To understand if CD15-3 is targeting cellular DHFR and thereby disrupting folA pathway, we further performed growth experiments in the presence of folA mix. folA mix which comprises of purine, thymine, glycine and methionine functions as a metabolic supplement for cells with diminished DHFR function (Singer et al., 1985). *E.coli* cells were grown in M9 media supplemented with “folA mix” under conditions of the presence and absence of CD15-3. We found that growth of CD15-3 treated cells was partially rescued by folA mix and the effect was more prominent at relatively lower concentrations of CD15-3 (Figure 6C).

At the same time, we observed only partial rescue of CD15-3 inhibited growth by folA mix or DHFR complementation at higher concentrations of CD15-3 suggesting that at high concentrations this compound might inhibit other proteins besides DHFR. In the subsequent publication we will use system-level approaches to discover possible additional targets of CD15-3, besides DHFR.

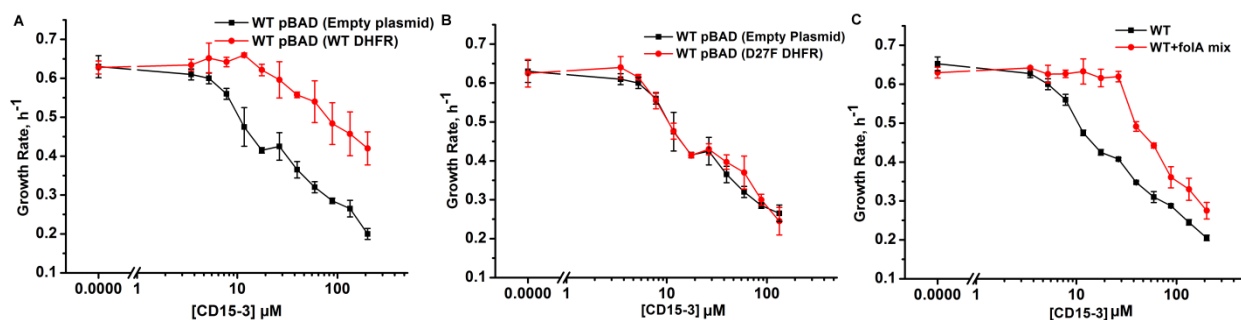


**Figure 6 Overexpression of functional (WT) DHFR shows partial recovery from CD15-3 induced growth inhibition.** (A) Overexpression of WT DHFR using pBAD-promoter and at 0.005% arabinose induction showed improvement in growth rates compared to cells with empty pBAD-plasmid (lacking DHFR gene) under conditions of CD15-3 treatment. (B) Comparative growth rate profiles of WT (with empty pBAD-promoter) and WT overexpressing D27F defunct mutant of DHFR. The growth rate profiles clearly show that D27F mutant of DHFR could not rescue cells from CD15-3 induced growth inhibition. (C) Comparative growth rate profiles of cells grown in presence of folA mix under conditions of CD15-3 treatment. Cells grown in presence of folA mix metabolic supplementation showed partial rescue in growth under conditions of CD15-3 treatment.

*CD15-3 largely prevents evolution of resistance in E. coli.*

The prime focus in our approach to design evolution drugs is on the search for inhibitors of a single protein target which would be equally effective against WT and resistant variants, and thus blocking possible escape routes for this target. To determine how fast WT *E. coli* can acquire resistance to CD15-3, we evolved *E. coli* under continuous exposure to the drug for over one month. We used a previously described automated serial passage protocol (Rodrigues and Shakhnovich, 2019) that adjusts the drug concentration in response to increase of growth rate caused by emergent resistant mutations thus maintaining evolutionary pressure to escape antibiotic stressor (see Methods and Materials section for details). We found that, at early stages of evolution, the CD15-3 concentration necessary to reduce the growth rate of the culture to 50% (with respect to non-inhibited naïve cells) increased to a value about 2.7 times higher than the  $IC_{50}$  of the naïve strain. However, at subsequent time points, the CD15-3 concentration remained constant, indicating that the cells were unable to further develop resistance to CD15-3. We found no mutations in the *folA* locus of the evolved strains upon Sanger sequencing analysis, indicating that the modest increase in resistance to CD15.3 is not associated with target modification. In parallel, we also studied evolution of resistance to TMP using the same approach. At the end of the evolutionary experiment, the cells evolved TMP resistance with  $IC_{50}$  two orders of magnitude greater than original naïve *E. coli* strain (Figure 7A). Sanger sequencing of the *folA* locus revealed one single point mutation (D27E) in the DHFR active site, which is associated with resistance to TMP (Oz et al., 2014).

To verify the results of evolutionary experiment, the population of cells evolved in presence of CD15-3 was further plated and two colonies were isolated. We measured growth of evolved variant of *E. coli* in M9 media using the same concentration range of CD15-3 as was used for WT cells. Evolved strains exhibited an  $IC_{50}$  for CD15-3 of  $131.5\mu\text{M}$ , about 2-fold higher compared to  $IC_{50}$  for WT (Figure 7B). Interestingly CD15-3 inhibited the D27E TMP escape mutant with  $IC_{50}$  close to naïve WT strain (Figure 7C).

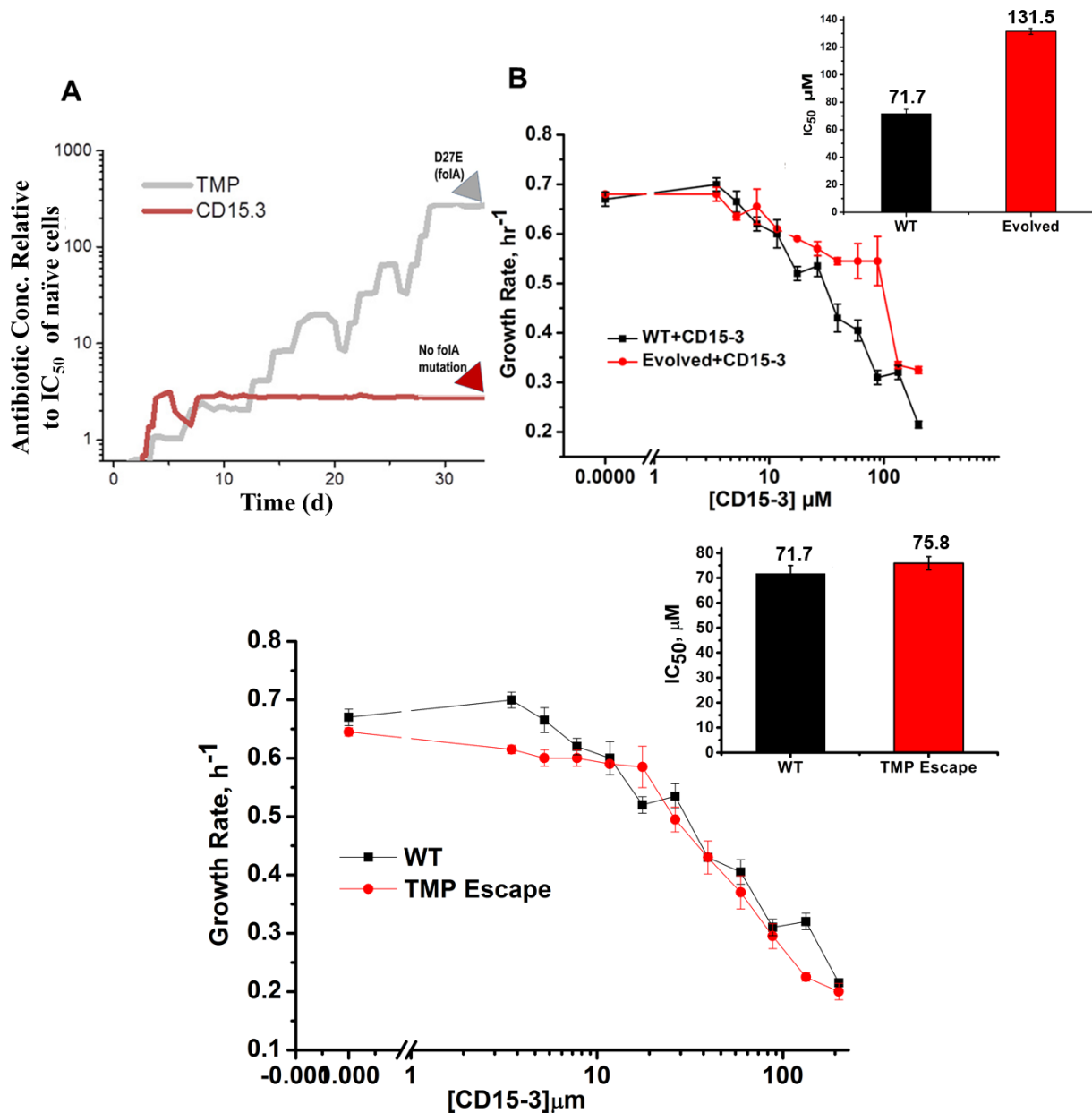


**Figure 7. Resistance to CD15-3 evolves slowly.** (A) Red and grey traces show evolution of antibiotic resistance against TMP and CD15-3. Under pressure from TMP cells evolved TMP resistance with  $IC_{50}$  two orders of magnitude greater than original naïve *E. coli* strain. Cells evolved under CD15-3 treatment showed an  $IC_{50}$  for CD15-3 of  $131.5 \mu M$  which is about 2-fold higher in comparison to  $IC_{50}$  for naïve WT. The antibiotic concentrations represented were obtained for a single evolutionary trajectory and are normalized to  $IC_{50}$  of naïve cells to TMP and CD15-3 ( $1.4$  and  $71.75 \mu M$  respectively). Cells which evolved under TMP treatment (TMP

*escape*) showed D27E mutation in the *folA* locus along with several other mutations outside of *folA*.

No mutation in the *folA* locus was observed in the CD15-3 evolved cells. (B) Growth rates in WT and evolved strain in a range of CD15-3 concentrations showing weak resistance of evolved strains. Inset shows the differences in IC<sub>50</sub> values in WT and evolved form. (C) CD15-3 also inhibits the growth of the TMP escape mutant with an IC<sub>50</sub> almost comparable to WT (naive).

#### *Whole Genome sequencing of the evolved variant*

We performed whole genome sequencing for the strains evolved under CD15-3 using two isolated colonies (mentioned as E1 and E2 in Figure. 8A) keeping naïve BW25113 strain as the reference strain sequence Surprisingly, no mutation associated in or upstream of *folA* locus was found. Therefore, the developed moderate resistance against CD15-3 could not be attributed to target modification.

Further analysis of the sequencing results revealed regions of duplication in the genome of the evolved strain as observed by the double depth-height (Figure.8A). Depth or coverage in sequencing outputs refer to the number of unique reads that include a given nucleotide in the sequence. The duplicated segment was found to be a stretch of above 81 KB. In the context of evolution of antibiotic resistance, the relatively frequent occurrence of genome duplications by amplification suggests that evolution of gene dosage can be a faster and more efficient mechanism of adaptation than rare downstream point mutations (Sandegren and Andersson, 2009). The gene that confers the limitation is often amplified in this mechanism, however, sometimes increased dosage of an unrelated non-cognate gene can resolve the problem.

Multiple genes belong to the region of genome duplication in the evolved strain (Figure. 8B) including transporter and efflux pump genes, transposable elements, stress response genes and metabolic genes viz. oxidoreductases, dehydrogenases, kinase regulators etc. The duplicated segment in the genome of the evolved variant contained genes encoding porin proteins, ABC transporter permeases and cation efflux pump genes (*cus*-genes). The CusCFBA system is a HME (heavy metal efflux)-RND system identified in *E. coli*. Resistance-nodulation-division (RND) family transporters refer to a category of bacterial efflux pumps primarily observed in Gram-negative bacteria. They are located in the membrane and actively transport substrates. Cus-efflux system was initially identified for the extrusion of silver (Ag<sup>+</sup>) and copper (Cu<sup>+</sup>). They have been found to induce resistance to fosfomycin (Nishino and Yamaguchi, 2001), dinitrophenol, dinitrobenzene, and ethionamide (Coutinho et al., 2010). The set of genes constituting *cus*-system viz. *cusCFBA*, are all located in the same operon (Gudipaty et al., 2012). The system is composed of the RND efflux pump (CusA); the membrane fusion protein, MFP (CusB); and of the outer membrane protein, OMP (CusC). The assembly of these proteins have been reported to be identical to the AcrB, CusA(3):CusB(6):CusC(3) (Delmar et al., 2013). In the duplicated segment of the evolved variant the entire *cus*-efflux system was found to be present.

We carried out the metabolic characterization of strains evolved in the presence of CD15.3 and naïve strains by LC-MS to further investigate the mechanism of resistance to the drug (a detailed analysis will be reported in a subsequent publication). Interestingly, our data revealed markedly lower abundance of the compound CD15-3 in the evolved strain compared to WT cells suggesting a possible efflux pump mediated compound depletion (Figure.8C). After four hours of CD15-3 treatment the abundance of the drug was found to be around 10 percent of the initial abundance. Drug efflux is a key mechanism of resistance in Gram-negative bacteria (Masi et al., 2017; Sandegren and Andersson, 2009). Pumping out drug compound under conditions of drug treatment is probably the most direct and nonspecific way of combating the toxic effect of a drug. It is interesting to note that we observed higher  $IC_{50}$  in the evolved strain compared to the naïve strain for some other antibiotics which we tested. Both the naïve and CD15-3 evolved cells were treated with TMP and Sulphamethoxazole. TMP inhibits bacterial DHFR while Sulphamethoxazole a sulfanilamide, is a structural analog of para-aminobenzoic acid (PABA) and binds to dihydropteroate synthetase. Under both the treatment conditions CD15-3 evolved cells partially escaped the drug inhibition and showed about 3-fold higher  $IC_{50}$  for TMP and Sulphamethoxazole (Figure 8D and E). These results show that the efflux mediated drug resistance in the evolved strain is non-specific. It demonstrates a potential strategy for antibiotic cross resistance and helps bacteria to escape inhibitory actions of CD15-3 and other antibacterial compounds with completely different protein targets. In the same vein we note that the efflux pump mechanism shows only moderate increase of  $IC_{50}$  for a variety of antibiotics in contrast to almost 1000-fold increase in strains evolved under TMP (Fig.7).



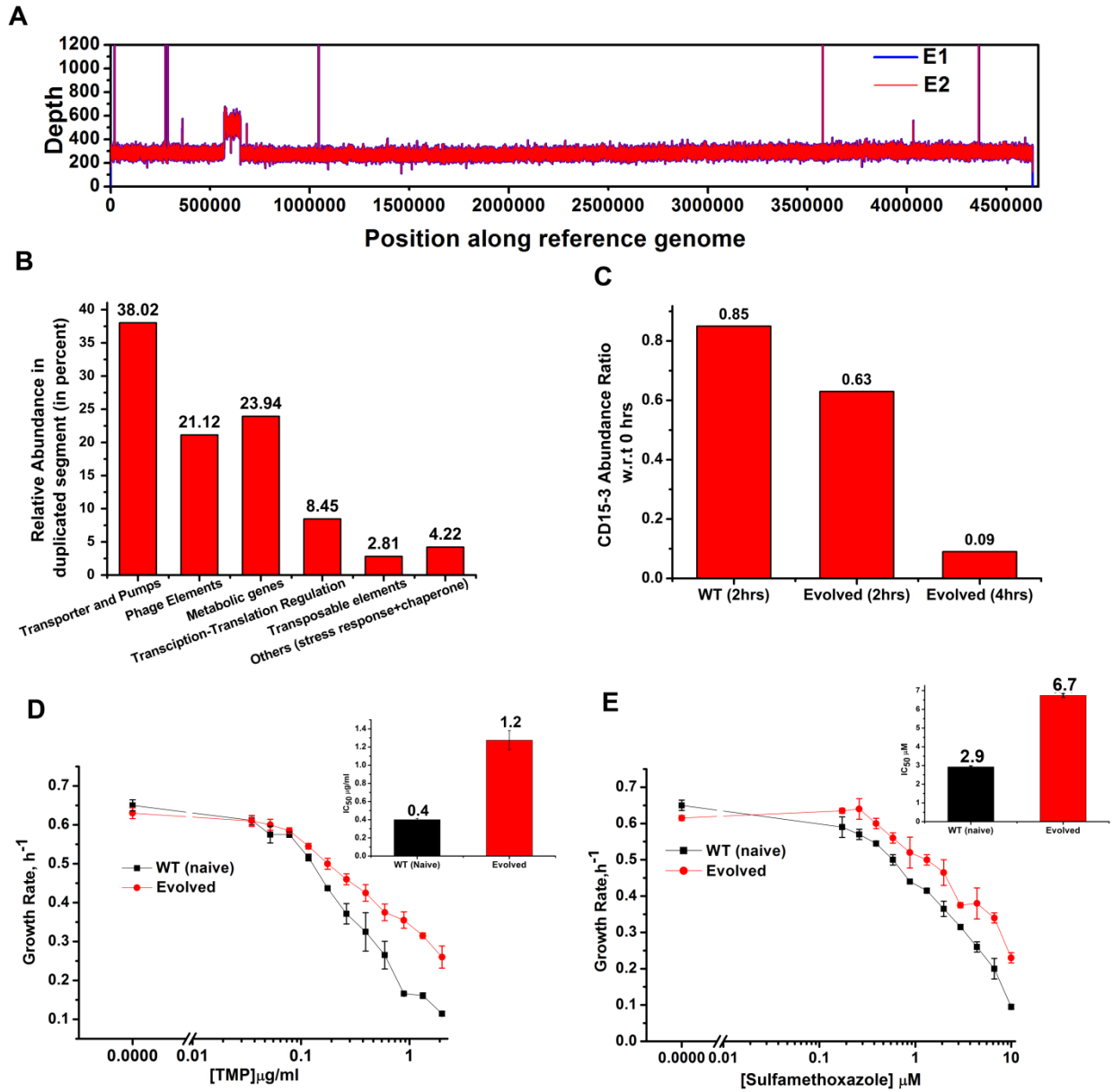


**Figure 8. Whole genome sequence of evolved variant revealed region of genome duplication.**

(A) Whole genome sequence display of the evolved form on alignment to BW25113 reference genome. The display shows regions of duplication as observed by increased height as per depth axis. (B) Bar plot showing the relative abundance of genes which constitutes duplicate segment in the genome of evolved form. (C) Bar plot showing the relative intracellular concentration of CD15-3 (with respect to the intracellular concentration in naïve cells at zero hour) in naïve and evolved strains at various time points of treatment. (D) CD15-3 evolved cells show cross resistance to other antibiotics. Growth rate profiles of WT (naïve) and CD15-3 evolved cells grown under varying concentrations of trimethoprim (TMP). CD15-3 evolved cells grow better

under TMP treatment and have almost 3 fold higher  $IC_{50}$  (shown in inset) compared to WT (naive). (E) Growth rate profiles of WT (naive) and CD15-3 evolved cells grown in presence of Sulfamethoxazole shows CD15-3 evolved cells grow better compared to WT (naive) cells (as reflected by the growth rates). CD15-3 evolved cells show somewhat higher  $IC_{50}$  compared to WT (naive) when grown in presence of Sulfamethoxazole (shown in in inset).

#### *Morphological changes induced by CD15-3 treatment*

As cellular filamentation and concomitant morphological changes are one of the visible hallmarks of stress responses to inhibition of proteins on the folate pathway of which DHFR is a member, (Ahmad et al., 1998; Justice et al., 2008; Sangurdekar et al., 2011; Zaritsky et al., 2006) we proceeded to image *E. coli* cells in absence of CD15-3 (control) and with added CD15-3. . Experiments were performed at 42 degrees Celsius. Cells were grown for 4 hours before image acquisition. DIC imaging results of the CD15-3 treated WT cells (Figure 9B) showed filamentation of the cells as compared to the cells grown in absence of CD15-3 (Figure 9A). Treated cells showed a wide distribution of cell length with a median length which was more than double than that in the untreated sets (Figure 9E).

Similar imaging experiment was also carried out for the CD15-3 resistant variant of *E. coli* cells obtained in our evolution experiment. These cells (Figure 9C) were found to have similar median cell lengths as WT (naïve) cells before CD15-3 treatment. Upon CD15-3 treatment these evolved cells showed slightly higher median cell length, although no visible filamentation was observed (Figure 9D). As efflux genes comprise 38% of the duplicated genome segment and CD15-3 abundance after 4 hours of treatment was markedly lower (compared to naïve WT) an efflux mediated drug resistance mechanism could potentially explain as to why evolved cells did not show any CD15-3 induced stressed morphology. The slight increase in median cell length in evolved cells upon treatment could be attributed to the fact that the transporter and efflux pump mediated resistance is a rather generic way to escape drug action and is not a perfect way to completely evade drug action.

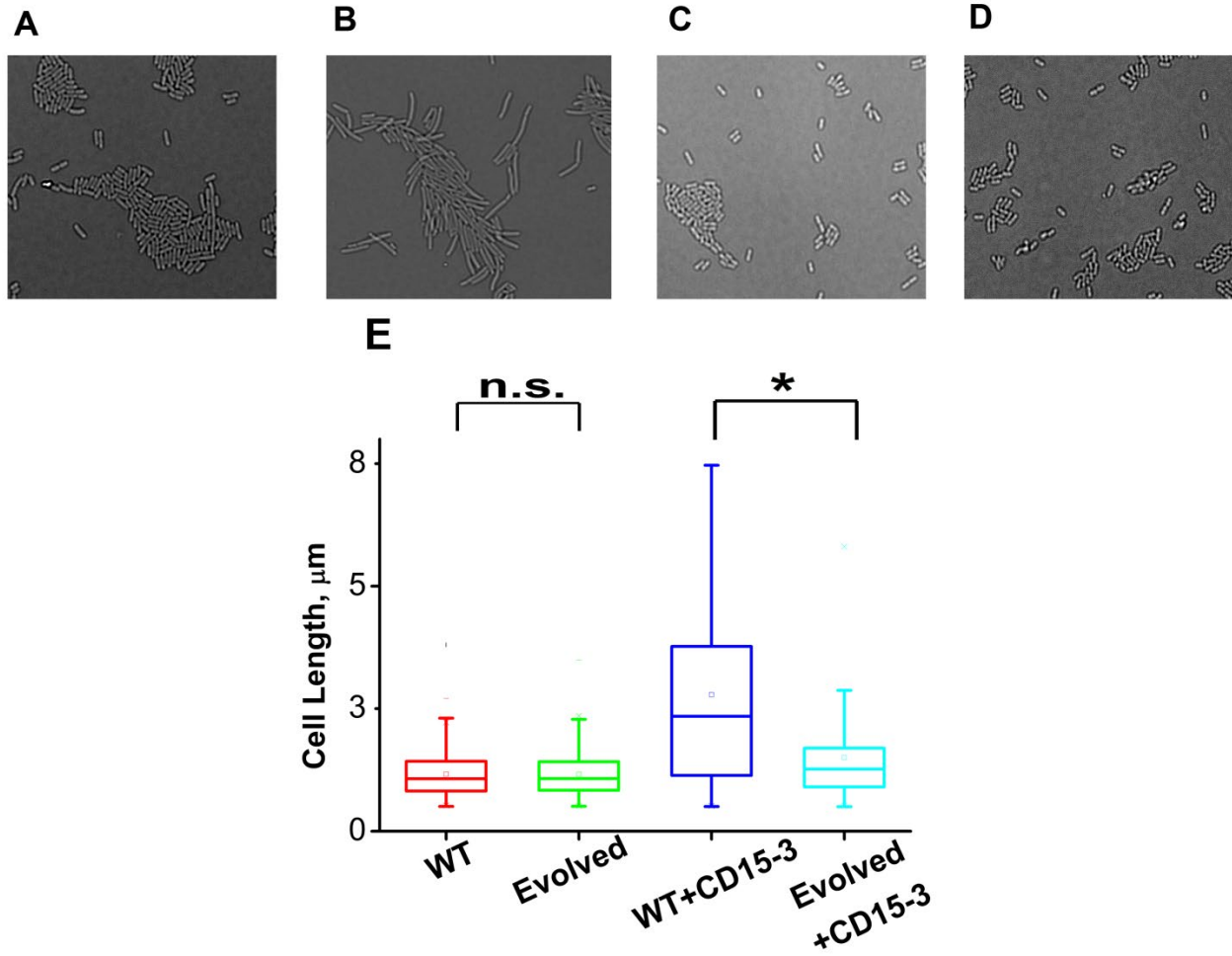


**Figure 9. CD15-3 treatment leads to stress induced morphological changes in WT *E. coli* cells.** DIC image of WT cells under (A) control (no CD15-3 treatment) and (B) treated (CD15-3 treatment) conditions. (C) DIC image of evolved *E. coli* cells under control (no CD15-3 treatment) and (D) CD15-3 treated condition. (E) Distribution of cell lengths as derived from DIC imaging of WT and evolved cells under control and CD15-3 treatment conditions. Untreated WT (naive) and evolved cells had comparable cell lengths with median cell lengths of 1.07  $\mu\text{m}$ . (n.s. indicates the distribution of cell lengths were not significantly different, Mann-Whitney test, p-value =0.961). Both WT and evolved cells were subjected to CD15-3 treatment at  $\text{IC}_{50}$  concentrations. WT treated cells were observed to have a filamentous morphology and the median cell length (2.343  $\mu\text{m}$ ) double of that of the untreated WT set. Evolved cells after CD15-3 treatment had a median cell length of 1.269  $\mu\text{m}$  which is slightly higher than that of untreated set. But the cell size distribution of the evolved cells showed much less change after CD15-3 treatment compared to that observed for the WT (\* indicates the distribution of cell lengths were significantly different, Mann-Whitney test, p-value <0.001).

## Discussion

Antibiotic resistance has emerged as a critical threat in the treatment of infectious diseases. This challenge is primarily an evolutionary problem which could be attributed to factors like antibiotic induced selection, the population structure of the evolving microbes and their genetics of adaptation (Roemhild and Schulenburg, 2019). Traditional antibiotic design protocols and development pipelines do not essentially consider this high intrinsic potential of bacterial adaptation in antibiotic stressed growth conditions and hence do not properly address the problems associated with drug resistance. This problem has taken an even more complicated shape with the emergence of multidrug resistant bacteria which can potentially escape the actions of a wide array of antibiotic formulations and have a complex landscape of evolutionary adaptation. To tackle these problems, complex treatment strategies for infectious diseases like combination-drug therapies or sequential drug therapies have been developed (Baym et al., 2016; Vestergaard et al., 2016). However, in many cases these strategies enjoyed only limited success in constraining the emergence of evolutionary escape variants and rare multidrug variants (Hegreness et al., 2008). Furthermore, none of these strategies act proactively by suppressing future evolutionary escape variants and remain more as a monotherapy or a combination therapy targeting WT variants. The current work presents a design protocol and a multi-tool drug development pipeline which addresses specifically the evolutionary issue by developing a strategy which aims at inhibiting both WT and evolutionary escape variants.

Antibiotics are generally designed to block the action of essential bacterial proteins thereby disrupting bacterial growth. As an important enzyme in the de novo pathway of amino acid, purine and thymidine synthesis, DHFR has long been regarded as a critical target for the development of antibiotic and anticancer drugs (Bharath et al., 2017; Lin and Bertino, 1991; Schweitzer et al., 1990). However rapid clinical resistance to available antifolates like TMP emerges merely after three rounds of directed evolution and sequential fixation of mutations through ordered pathways has been shown to contribute to the evolutionary paths for antibiotic resistance (Tamer et al., 2019; Toprak et al., 2012). Even though several classes of small molecules have been investigated for their potential antifolate activity, the rapid emergence of resistance by readily accessible mutational pathways in the *folA* gene pose an immense challenge (Toprak et al., 2012). It is thus urgent to develop new tools for the systematic identification of novel scaffolds and discovery of inhibitors that interact simultaneously with both WT DHFR and antifolate resistant DHFR mutants. By an efficient virtual screening protocol to scan large databases, two hits of novel scaffolds were identified, which showed inhibitory activity against both WT and resistant mutant forms of DHFR. Unlike conventional approaches primarily focused on chemical synthesis of derivatives based on known inhibitor scaffolds (Francesconi et al., 2018; Hopper et al., 2019; Lam et al., 2014; Reeve et al., 2016), we deployed an efficient novel multi-tier approach to come up with chemically novel inhibitors. To further improve DHFR inhibitory activity of the two hits, a rapid round of compound optimization was conducted through a structural similarity search. This approach turned out to be very effective as we tested only 12 candidate compounds and found CD15-3 with improved antimicrobial activity against both the WT and trimethoprim-resistant DHFR mutant *E. coli* strains. Among trimethoprim-resistant mutations, P21L, A26T, L28R, and their combinations are

identified as an interesting set that recurrently appeared in two out of five independent evolution experiments, and their order of fixation in both cases was similar (Toprak et al., 2012). Fitness landscape of TMP resistance showed that the L28R variant exhibits the highest resistance among all three single mutants (Rodrigues et al., 2016). Introduction of another mutation on the L28R background, either P21L or A26T, does not change  $IC_{50}$  significantly (Rodrigues et al., 2016; Toprak et al., 2012). Thermal denaturation experiments demonstrate that L28R mutation is stabilizing showing an increase in  $T_m$  of 6 °C above WT DHFR, in contrast to the destabilizing mutations P21L and A26T (Rodrigues et al., 2016). In addition, the L28R mutation cancels out the destabilization brought by P21L and A26T, restoring the  $T_m$  of the double and triple mutants to WT values. The L28R mutation also shows improved compactness, inferred from its reduced bis-ANS binding (Rodrigues et al., 2016). Thus, among the evolved mutant *E. coli* strains, L28R is one of the most frequently encountered resistance mutations in *folA* gene which render traditional anti-folate drugs like TMP clinically ineffective (Rodrigues et al., 2016; Toprak et al., 2012). Effectively L28R serves as a stability “reservoir” providing a gateway to multiple evolutionary trajectories leading to resistance. The discovered DHFR inhibitor CD15-3 shows about 18-fold better efficacy than that of TMP on L28R *E. coli* variant strain, indicating its potential in combating resistance conferred by gateway point mutations of DHFR.

Our in vivo DHFR over-expression experiment showed partial recovery from the CD15-3 induced growth inhibition, thereby validating DHFR as a target for the intracellular inhibition by CD15.3. That DHFR is being targeted by CD15-3 is further supported by our imaging results showing antibiotic-stress induced filamentation in the WT cells, a clear sign indicating that the folate pathway is indeed impacted by the drug (Bhattacharyya et al., 2019). However, the *partial* recovery upon DHFR overexpression strongly suggests the presence of at least one additional protein target of CD15-3. As CD15-3 was designed to allow interaction with both WT and “modified” active site pockets in the mutant forms of DHFR, this might make CD15-3 active against other enzymes that bind structurally similar substrates, most likely of the folate pathway. In the subsequent work we will present integrative metabolomic analysis that allowed us to identify additional targets of CD15-3.

As resistant mutants arise under selection pressure induced by stressor drugs, a prime objective behind our effort to design novel evolution drug was to block these escape routes. We carried a 30-day long evolution experiment to evolve CD15-3 resistant cells. Unlike TMP resistance which emerged quickly and resulted in strains having almost 1000-fold higher  $IC_{50}$ , CD15-3 resistant cell achieved an  $IC_{50}$  which was only 2.7 times greater than that observed in WT. Further our whole genome sequence analysis revealed that there was no mutation in the target *folA* gene. Rather, we found that partial genome duplication was responsible for evolution of modest resistance against CD15-3. Transporters and efflux pump genes were disproportionately represented in the duplicated segment. Efflux pump driven resistance is potentially a plausible first escape strategy to evade drug actions and a generic way to evolve resistance. The importance of efflux pump genes and transporters as first line of defence against antibiotic stressors was shown in studies where deletion of such genes leads to inferior mutational paths and escape strategies (Lukačšínová et al., 2020). The modest resistance phenotype observed with CD15-3 evolved cells can hence be attributed to a more generic phenomenon of drug efflux

and not target modification as observed with traditional anti-folate drug like TMP. This could be potentially attributed to the multivalent nature of CD15-3. TMP specifically interacts with DHFR and hence mutation in the target loci (*folA*) provides optimal solution to escape the TMP stress. As CD15-3 potentially interacts with more than one target apart from DHFR, point mutations in one of the target proteins do not provide optimal solutions. While point mutations at multiple target loci can complicate the evolutionary fitness landscape, efflux mediated resistance on the other hand provides a generic and rapid rescue strategy bypassing the possibilities of multiple point mutations. However, this strategy apparently has its drawback as overexpression of additional pumps can incur fitness cost and lead to only modest 2-3 fold increase in  $IC_{50}$ .

Bacterial fitness/adaptation landscape under conditions of antibiotic induced stress could be extremely complicated with multiple escape strategies. The method and the plausible solutions we have presented here considers the common antifolate evolutionary escape route which happens by target modification. CD15-3 was found to be effective in inhibiting the most potent DHFR escape mutants along with the WT form. Surprisingly, we observed CD15-3 was equally effective in inhibiting the growth of the TMP escape mutant D27E which emerged in our evolution experiment under TMP stress.

CD15-3 resistance mechanism appears to be efflux driven. Pumps can be considered as evolutionary capacitors which store and release adaptive variations under conditions of stress. Efflux pumps have been reported to contribute to the rise in the mutation rates by influencing growth alone or by exporting compounds which participate in cell-to-cell interactions and the methyl cycle (Cirz et al., 2005). As CD15-3 is designed to block escape routes associated with *folA* mutations, resistance ensues with the generic efflux mediated escape route. Higher gene dosage of transporters and pumps has its own fitness cost potentially providing an interim evolutionary solution to the challenge of antibiotic stress. Evolution on a much longer time scale might reveal novel escape routes associated with other genes on and/or off-target. Exploration of long term evolutionary mechanism of potential escape from CD15-3 can help us understand the complexity of fitness landscape for this novel prospective antibiotic. This can further help in refining the drug development protocol which can also address the issue of efflux mediated evolutionary escape routes. A plausible futuristic anti-evolution strategy could be using combination of potential evolution drug formulations like CD15-3 and adjuvants which could block the pumps, thereby potentially also obstructing the generic escape routes. We suggest that the currently popular drug development protocols could be sub-optimal as they overlook ways to limit bacterial adaptation.

As a caveat we note that novel compounds discovered here, while promising as candidates for new class of anti-evolution antibiotics, represents only initial leads in the drug development pipeline. A detailed characterization of pharmacokinetics of the prospective compounds using the standard approaches adopted in pharmaceutical industry need to be carried out to establish their plausibility as drug candidates. However, our approach that integrates computational and in vitro experimental components in a mutual feedback loop allows considerable power and flexibility in optimization of emerging compounds potentially significantly shortening the development cycle.

To summarize, we believe that our comprehensive multiscale-multitool approach to address the clinically challenging issue of antibiotic resistance and the discovered CD15-3 can be an attractive starting point for further optimization and development of evolution drugs and adopting a broad strategy to combat evolution of drug resistance.

## 2. Methods and Materials

### *Preparation of Databases and Proteins*

Two commercially available databases ChemDiv (<http://www.chemdiv.com/>, about 1.32 million compounds) and Life Chemicals (<http://www.lifechemicals.com/>, about 0.49 million compounds) were selected for virtual screening. Both databases contain a large amount of diverse structures which are useful as potential hits for drug development and providing integrative drug discovery strategies for pharmaceutical and biotech companies (Zhang et al., 2015). In addition, the known *E. coli* DHFR inhibitors (183 compounds) with  $IC_{50}$  values ranging from 1 nM to 100  $\mu$ M were downloaded from BindingDB (<https://www.bindingdb.org/bind/index.jsp>) (Liu et al., 2006) used as a reference database. All compounds from the two databases were added hydrogens and then optimized by a user-defined protocol in Pipeline Pilot (Warr, 2012). A couple of physicochemical properties including molecular weight, AlogP, number of hydrogen donors (HBD) and acceptors (HBA), number of rings, aromatic rings, rotatable bonds and molecular fractional polar surface area (Molecular\_FPSA) were calculated in Pipeline Pilot (Warr, 2012) using the Calculate Molecular Properties protocol. All the compounds were further prepared by the LigPrep module in Maestro 10.2 in Schrodinger (Steffan and Kuhlen, 2001) to ensure they were appropriate for molecular docking.

### *Molecular Docking*

All *E. coli* DHFR crystal structures (issued before 09-10-2016) were downloaded from Protein Data Bank (PDB) (Berman et al., 2006) and classified into three categories. Among them four representatives including PDB 1RX3 (M20 loop closed), 1RA3 (M20 loop open), 1RC4 and 5CCC (M20 loop occluded) were selected for molecular docking and molecular dynamics studies. All these protein structures were prepared by the Protein preparation wizard in Maestro 10.2 of Schrodinger (Madhavi Sastry et al., 2013) to add hydrogens and missing atoms and to minimize the energy. All water molecules in the original crystal structures were removed except the 302<sup>th</sup> H<sub>2</sub>O which is located in the active site and forms a key hydrogen bond with the cognate ligand. Hydrogen atoms and partial charges were added to the protein, and then a restrained minimization of only the hydrogens was conducted. A grid box centered on the cognate ligand was generated by the Receptor Grid Generation module in Schrodinger. To soften the potential for nonpolar parts of the receptors, one can scale the van der Waals radii (scaling factor set to 1.0) of the receptors with partial atomic charge less than the specified cutoff (set to 0.25Å). Due to its excellent performance through a self-docking analysis (Zhang et al., 2017; Zhang et al.), the Glide module in Schrodinger was selected for molecular simulations. All three precision modes including the high throughput virtual screening (HTVS), the standard precision (SP) and the extra precision (XP) were utilized sequentially according to their speed and accuracy. For each

docking run, the 10 best poses of each ligand were minimized by a post docking program with the best pose saved for further analysis and the root mean standard deviation (RMSD) between the output and input structures were calculated.

### *Molecular Dynamics*

Protein-compound complexes resulted from molecular docking were employed for molecular dynamics simulation. Proteins were prepared using the Protein Preparation Wizard (Madhavi Sastry et al., 2013) tool of Maestro in Schrodinger by adding missing atoms and hydrogens and minimizing the energy. Ligands were preprocessed by assigning the correct protonation state using Chimera 1.9 (Pettersen et al., 2004). Then, they were optimized by an implicit water model under the M06-2X/6-31+G\*\* level of theory and their RESP charges were computed at the HF/6-31G\* level of theory using Gaussian 09 (Chai and Head-Gordon, 2009). Finally, their ligand topologies were generated by acpype which is an interface to antechamber (Wang et al., 2006). The TIP3P water model (Jorgensen, 1981) and AMBER03 force field (Chillemi et al., 2010) were used for the simulation using GPU processors with GROMACS, version 5.0.2 (Spoel et al., 2005). Firstly, the system was solvated in a water filled rhombic dodecahedron box with at least 12 Å distance between the complex and box edges. Then, the charges of system were neutralized by adding counter ions (Na<sup>+</sup> or Cl<sup>-</sup>) by the genion tool in Gromacs. The system was then relaxed through an energy minimization process with steepest descent algorithm first, followed by a conjugate gradient algorithm. The energy of the system was minimized until the maximum force reached 5.0 kJ mol<sup>-1</sup> nm<sup>-1</sup>. After a primary constraint NVT simulation of 200 ps with protein atoms being fixed at 100 K, an NVT simulation of 400 ps without restraints was performed with simulated annealing at the temperature going from 100 to 300K linearly. Then we performed an NPT simulation of 500 ps to equilibrate the pressure. Eventually, a production MD was conducted for 10 ns at 300 K twice. Bond lengths were constrained using LINCS algorithm during the simulation (Hess, 2008). It is commonly accepted that nanosecond MD simulations are reliable to investigate local conformational changes (Yeggoni et al., 2014). Thus, the last 2 ns of each 10 ns production simulation were extracted at every 10 ps interval (400 snapshots in total) for calculating the molecular mechanics/Poisson-Boltzmann surface area binding energy (MM-PBSA) by the AMBER12 package (Miller et al., 2012). Average energy for 400 snapshots was saved for binding free energy calculation using MMPBSA (Cheron and Shakhnovich, 2017). More details about this protocol are described elsewhere (Cheron and Shakhnovich, 2017).

### *Enzymatic Activity Assay*

All reagents and chemicals were of high quality and were procured from Sigma-Aldrich Co., USA, Amresco, or Fisher Scientific. According to our former study, wild-type (WT) *E.coli*, *C. muridarum* and *L. grayi* DHFR as well as mutant *E. coli* DHFR proteins including P21L, A26T and L28R point mutants were expressed and purified in the same way as previously described (Rodrigues et al.; Rodrigues et al., 2016). The inhibitory activity of the hit compounds against DHFR was evaluated according to our previous protocol (Rodrigues et al., 2016). At fixed substrate concentration 100µM NADPH and 30µM dihydrofolate, inhibition constants were determined from kinetic competition experiments performed based on varying inhibitor



concentrations (Srinivasan and Skolnick, 2015). Spectrophotometric assay on 96-well multiplate reader at 25 °C was conducted by monitoring the conversion of NADPH as a decrease in absorbance at 340 nm for 180 s. Through a molar-extinction coefficient ( $\epsilon$ ) of  $6.2 \times 10^4 \text{ M}^{-1} \text{ cm}^{-1}$  for  $\beta$ -NADPH at 340 nm, the amount of product formed was calculated and the nonenzymatic hydrolysis of NADPH was normalized. The DHFR enzyme was added to initiate the reaction, and the initial velocities with product formation less than 5% were measured for reaction mixtures containing 100 mM HEPES, pH 7.3, at  $\sim 22^\circ\text{C}$ . The concentration-dependent inhibition curves were determined in 100 mM HEPES, pH 7.3, 50  $\mu\text{M}$  DHF, 60  $\mu\text{M}$  NADPH, and variable concentration of each inhibitor. The enzyme concentration was 16.7 nM. The curves were fit to

the equation  $y = \frac{100\%}{(1 + I / IC_{50})}$ , where I is concentration of the inhibitor and y is the percentage

of catalytic activity of DHFR. The values of inhibition constant  $K_i$  were obtained by fitting a competitive inhibition equation (Krohn and Link, 2003) from plots of activity vs. inhibitor

concentration using the equation  $K_i = \frac{IC_{50}}{1 + \frac{[S]}{K_M}}$ , where the  $K_M$  values of DHFR enzyme for both

substrates (DHF and NADPH) have been measured before (Rodrigues et al., 2016) and [S] is the substrate concentration of DHF. The concentration of the test hits was varied to obtain  $IC_{50}$  values and then converted to  $K_i$  values. The concentration of the substrate DHF is fixed at 50  $\mu\text{M}$  (Rodrigues et al., 2016) All the measurements were conducted in duplicate, and the error values are indicated by standard errors. All the data were fit using the nonlinear curve-fitting subroutines OriginPro (Seifert and E., 2014).

#### *Bacterial Growth Measurements and Determination of $IC_{50}$ values*

Cultures in M9 minimal medium was grown overnight at 37 °C and were then normalized to an OD of 0.1 using fresh medium. A new normalization to an OD=0.1 was conducted after additional growth during 5–6 h. Then, the M9 medium and six different concentrations of the positive control TMP and all hit compounds in the 96-well plates (1/5 dilution) were incubated. The incubation of the plates was performed at 37 °C and the orbital shaking and absorbance measurements at 600 nm were taken every 30 min during 15 h. By integration of the area under the growth curve (OD vs. time), the growth was quantified between 0 and 15 h, as described elsewhere (Palmer et al., 2015). For the WT DHFR or a given mutant, the growth integrals normalized by corresponding values of growth for that same strain without the hit compounds. By fitting a logistic equation to plots of growth vs. compound concentrations, the  $IC_{50}$  values were determined. The reported  $IC_{50}$  values are an average based on at least three replicates and standard errors are indicated.

#### *Whole Genome sequencing*

Using single isolated colonies, whole genome sequencing for the evolved variants was performed resorting to Illumina MiSeq 2 x 150 bp paired-end configuration (Novogene). We

used breqseq pipeline (Deatherage et al., 2014) on default settings, using the *E. coli* K-12 substr. BW25113 reference genome (GenBank accession no. [CP009273.1](#)).

### *Evolution experiments*

Evolution of *E. coli* strains in the presence of prospective compound CD15-3 or TMP was carried out by serial passaging using an automated liquid handling system (Tecan Freedom Evo 150), a procedure similar to the one described previously (Rodrigues and Shakhnovich, 2019). In this setup, cultures are grown in wells of a 96-well microplate, and the optical density (600 nm) is measured periodically using a plate reader (Tecan Infinite M200 Pro). In each serial passage, the cultures are diluted with fresh growth media into the wells of the adjacent column. The growth rate measured for each culture at a given passage is compared with the growth rate determined in the absence of antibiotic and the concentration of antibiotic is increased by a factor of 2 if it exceeds (75 %), otherwise maintained. To avoid excessive antibiotic inhibition, the concentration was increased only once in every two consecutive passages. This procedure forces cells to grow under sustained selective pressure at growth rates close to 50% of that of non-inhibited cells.

### *Differential interference contrast (DIC)*

WT cells were grown in M9 media supplemented with  $0.8\text{gL}^{-1}$  glucose and casamino acids (mixtures of all amino acids except tryptophan) in absence and presence of CD15-3 at  $42^{\circ}\text{C}$  for incubation and 300 rpm constant shaking. Drop in DHFR activity has been associated with cellular filamentation and similar phenotype is observed under TMP treatment (Bhattacharyya et al., 2019). Since CD15-3 targets intracellular DHFR and soluble fraction of cellular DHFR is lower at 42 degrees C we chose this temperature for our imaging studies (Bershtein et al., 2012).

Aliquots were taken from the growing culture and they were drop casted on agar bed/blocks. These blocks were taken further processed for differential inference contrast (DIC) imaging using Zeis Discovery imaging workstation. Multiple fields were observed and scanned for a single condition type and a minimum of three replicates were used for imaging studies. Similar methods for imaging were used for evolved cell types under conditions of absence and presence of CD15-3 compound. Intellesis Module was used for analyzing DIC images. On average, around 500 cells were analyzed for computing cell length. *E. coli* cell lengths in our imaging studies were not normally distributed. Nonparametric Mann-Whitney test was therefore used to determine if the cell length distributions were significantly different upon CD15-3 treatment.

**Acknowledgement** This work was supported by NIH RO1 068670 and by the program of China Scholarship Council (CSC). We are grateful to Nicolas Chéron and Jiho Park for help with the computational setup.

## References

- Ahmad, S., Kirk, S., and Eisenstark, A. (1998). Thymine metabolism and thymineless death in prokaryotes and eukaryotes. *Annual review of microbiology* *52*, 591-625.
- Baell, J.B., and Holloway, G.A. (2010). New substructure filters for removal of pan assay interference compounds (PAINS) from screening libraries and for their exclusion in bioassays. *Journal of medicinal chemistry* *53*, 2719-2740.
- Baym, M., Stone, L.K., and Kishony, R. (2016). Multidrug evolutionary strategies to reverse antibiotic resistance. *Science* *351*.
- Berman, H.M., Westbrook, J., Feng, Z., Gillil, G., Bhat, T.N., Weissig, H., Shindyalov, I.N., and Bourne, P.E. (2006). The Protein Data Bank, 1999&ndash.
- Bershtein, S., Mu, W., and Shakhnovich, E.I. (2012). Soluble oligomerization provides a beneficial fitness effect on destabilizing mutations. *Proceedings of the National Academy of Sciences* *109*, 4857-4862.
- Bharath, Srinivasan, João, V., Rodrigues, Sam, Tondast-Navaei, Eugene, Shakhnovich, and Jeffrey (2017). Rational Design of Novel Allosteric Dihydrofolate Reductase Inhibitors Showing Antibacterial Effects on Drug-Resistant *Escherichia coli* Escape Variants. *Acs Chem Biol* *18*48-1857, *12*.
- Bhattacharyya, S., Bershtein, S., Adkar, B.V., Woodard, J., and Shakhnovich, E.I. (2019). A case of 'mistaken identity': structurally similar ligand inhibits Thymidylate Kinase causing reversible filamentation of *E. coli*. *bioRxiv*, 738823.
- Bhattacharyya, S., Bershtein, S., Yan, J., Argun, T., Gilson, A.I., Trauger, S.A., and Shakhnovich, E.I. (2016). Transient protein-protein interactions perturb *E. coli* metabolome and cause gene dosage toxicity. *Elife* *5*, e20309.
- Bleyer, W.A. (2015). The clinical pharmacology of methotrexate: new applications of an old drug. *Cancer* *41*, 36-51.
- Carroll, M.J., Mauldin, R.V., Gromova, A.V., Singleton, S.F., Collins, E.J., and Lee, A.L. (2012). Evidence for dynamics in proteins as a mechanism for ligand dissociation. *Nature chemical biology* *8*, 246-252.
- Chai, J.D., and Head-Gordon, M. (2009). Long-range corrected double-hybrid density functionals. *Journal of Chemical Physics* *131*, 174105.
- Cheron, N., and Shakhnovich, E.I. (2017). Effect of sampling on BACE-1 ligands binding free energy predictions via MM-PBSA calculations. *J Comput Chem* *38*, 1941-1951.
- Chillemi, G., Coletta, A., Mancini, G., Sanna, N., and Desideri, A. (2010). An amber compatible molecular mechanics force field for the anticancer drug topotecan. *Theoretical Chemistry Accounts* *127*, 293-302.
- Cirz, R.T., Chin, J.K., Andes, D.R., de Crécy-Lagard, V., Craig, W.A., and Romesberg, F.E. (2005). Inhibition of mutation and combating the evolution of antibiotic resistance. *PLoS Biol* *3*, e176.
- Coutinho, H.D., Costa, J.G., Lima, E.O., Falcao-Silva, V.S., and Siqueira-Júnior, J.P. (2010). Increasing of the aminoglycoside antibiotic activity against a multidrug-resistant *E. coli* by *Turnera ulmifolia* L. and chlorpromazine. *Biological Research for Nursing* *11*, 332-335.
- Delmar, J.A., Su, C.-C., and Edward, W.Y. (2013). Structural mechanisms of heavy-metal extrusion by the *Cus* efflux system. *Biometals* *26*, 593-607.
- Finland, M., and Kass, E.H. (1973). Trimethoprim-sulfamethoxazole. Summary and comments on the conference. *Journal of Infectious Diseases* *128*, Suppl:792.
- Francesconi, V., Giovannini, L., Santucci, M., Cichero, E., Costi, M.P., Naesens, L., Giordanetto, F., and Tonelli, M. (2018). Synthesis, biological evaluation and molecular modeling of novel azaspiro dihydrotriazines as influenza virus inhibitors targeting the host factor dihydrofolate reductase (DHFR). *European journal of medicinal chemistry* *155*, 229-243.

Gudipaty, S.A., Larsen, A.S., Rensing, C., and McEvoy, M.M. (2012). Regulation of Cu (I)/Ag (I) efflux genes in *Escherichia coli* by the sensor kinase CusS. *FEMS microbiology letters* *330*, 30-37.

Hegreness, M., Shoresh, N., Damian, D., Hartl, D., and Kishony, R. (2008). Accelerated evolution of resistance in multidrug environments. *Proceedings of the National Academy of Sciences* *105*, 13977-13981.

Hess, B. (2008). P-LINCS: A parallel linear constraint solver for molecular simulation. *Journal of Chemical Theory and Computation* *4*, 116-122.

Hopper, A.T., Brockman, A., Wise, A., Gould, J., Barks, J., Radke, J.B., Sibley, L.D., Zou, Y., and Thomas, S. (2019). Discovery of Selective *Toxoplasma gondii* Dihydrofolate Reductase Inhibitors for the Treatment of Toxoplasmosis. *Journal of Medicinal Chemistry* *62*, 1562-1576.

Huovinen, P., Sundström, L., Swedberg, G., and Sköld, O. (1995). Minireview. Trimethoprim and sulfonamide resistance. *Antimicrobial Agents & Chemotherapy* *39*, 279-289.

Izbicka, E., Diaz, A., Streeper, R., Wick, M., Campos, D., Steffen, R., and Saunders, M. (2009). Distinct mechanistic activity profile of pralatrexate in comparison to other antifolates in in vitro and in vivo models of human cancers. *Cancer Chemotherapy & Pharmacology* *64*, 993-999.

Jorgensen, W.L. (1981). Transferable Intermolecular Potential Functions for Water, Alcohols, and Ethers. Application to Liquid Water. *Jamchemsoc* *103*.

Justice, S.S., Hunstad, D.A., Cegelski, L., and Hultgren, S.J. (2008). Morphological plasticity as a bacterial survival strategy. *Nature Reviews Microbiology* *6*, 162-168.

Krohn, K.A., and Link, J.M. (2003). Interpreting enzyme and receptor kinetics: keeping it simple, but not too simple. *Nuclear Medicine & Biology* *30*, 0-826.

Kumar, A. (2011). Investigation of structures similarity of organic substances. *Resonance* *16*, 61-64.

Lam, T., Hilgers, M.T., Cunningham, M.L., Kwan, B.P., Nelson, K.J., Brown-Driver, V., Ong, V., Trzoss, M., Hough, G., Shaw, K.J., *et al.* (2014). Structure-Based Design of New Dihydrofolate Reductase Antibacterial Agents: 7-(Benzimidazol-1-yl)-2,4-diaminoquinazolines. *Journal of Medicinal Chemistry* *57*, 651-668.

Leonardo, F., Ricardo, D.S., Glaucius, O., and Adriano, A. (2015). Molecular Docking and Structure-Based Drug Design Strategies. *Molecules* *20*, 13384-13421.

Lin, J.T., and Bertino, J.R. (1991). Clinical Science Review: Update on Trimetrexate, a Folate Antagonist with Antineoplastic and Antiprotozoal Properties. *Cancer Investigation* *9*, 159-172.

Liu, F.T., Li, N.G., Zhang, Y.M., Xie, W.C., Yang, S.P., Lu, T., and Shi, Z.H. (2020). Recent advance in the development of novel, selective and potent FGFR inhibitors. *European journal of medicinal chemistry* *186*, 111884.

Liu, T., Lin, Y., Xin, W., Jorissen, R.N., and Gilson, M.K. (2006). BindingDB: a web-accessible database of experimentally determined protein–ligand binding affinities. *Nucleic Acids Research*, suppl\_1.

Lukačšínová, M., Fernando, B., and Bollenbach, T. (2020). Highly parallel lab evolution reveals that epistasis can curb the evolution of antibiotic resistance. *Nature communications* *11*, 1-14.

Madhavi Sastry, G., Adzhigirey, M., Day, T., Annabhimoju, R., and Sherman, W. (2013). Protein and ligand preparation: parameters, protocols, and influence on virtual screening enrichments. *Journal of Computer-Aided Molecular Design* *27*, 221-234.

Manto, C.C., Sara, M., and Laleh, A. (2018). Drug Metabolites and their Effects on the Development of Adverse Reactions: Revisiting Lipinski's Rule of Five. *International Journal of Pharmaceutics* *549*, 133-149.

Marcou, G., and Rognan, D. (2007). Optimizing fragment and scaffold docking by use of molecular interaction fingerprints. *Journal of Chemical Information & Modeling* *47*, 195-207.

Masi, M., Réfregiers, M., Pos, K.M., and Pagès, J.-M. (2017). Mechanisms of envelope permeability and antibiotic influx and efflux in Gram-negative bacteria. *Nature microbiology* *2*, 1-7.

Miller, B.R., McGee, T.D., Swails, J.M., Homeyer, N., Gohlke, H., and Roitberg, A.E. (2012). MMPBSA.py: An Efficient Program for End-State Free Energy Calculations. *Journal of Chemical Theory and Computation* 8, 3314-3321.

Oz, T., Guvenek, A., Yildiz, S., Karaboga, E., Tamer, Y.T., Mumcuyan, N., Ozan, V.B., Senturk, G.H., Cokol, M., Yeh, P., *et al.* (2014). Strength of selection pressure is an important parameter contributing to the complexity of antibiotic resistance evolution. *Mol Biol Evol* 31, 2387-2401.

Palmer, A.C., Toprak, E., Baym, M., Kim, S., and Kishony, R. (2015). Delayed commitment to evolutionary fate in antibiotic resistance fitness landscapes. *Nature communications* 6, 7385.

Peneş, N.O., Muntean, A.A., Moisoiu, A., Muntean, M.M., Chirca, A., Bogdan, M.A., and Popa, M.I. (2017). An overview of resistance profiles ESKAPE pathogens from 2010-2015 in a tertiary respiratory center in Romania. *Rom J Morphol Embryol* 58, 909-922.

Petterson, E.F., Goddard, T.D., Huang, C.C., Couch, G.S., Greenblatt, D.M., Meng, E.C., and Ferrin, T.E. (2004). UCSF Chimera—A visualization system for exploratory research and analysis. *Journal of Computational Chemistry* 25, 1605-1612.

Reeve, S.M., Scocchera, E., Ferreira, J.J., N, G.D., Keshipeddy, S., Wright, D.L., and Anderson, A.C. (2016). Charged Propargyl-Linked Antifolates Reveal Mechanisms of Antifolate Resistance and Inhibit Trimethoprim-Resistant MRSA Strains Possessing Clinically Relevant Mutations. *J Med Chem* 59, 6493-6500.

Rodrigues, J.O.V., Bershtein, S., Li, A., Lozovsky, E.R., Hartl, D.L., and Shakhnovich, E.I. Biophysical principles predict fitness landscapes of drug resistance. *Proceedings of the National Academy of Sciences*, 201601441.

Rodrigues, J.V., Bershtein, S., Li, A., Lozovsky, E.R., Hartl, D.L., and Shakhnovich, E.I. (2016). Biophysical principles predict fitness landscapes of drug resistance. *Proc Natl Acad Sci U S A* 113, E1470-1478.

Rodrigues, J.V., and Shakhnovich, E.I. (2019). Adaptation to mutational inactivation of an essential gene converges to an accessible suboptimal fitness peak. *Elife* 8, e50509.

Roemhild, R., and Schulenburg, H. (2019). Evolutionary ecology meets the antibiotic crisis: Can we control pathogen adaptation through sequential therapy? *Evolution, medicine, and public health* 2019, 37-45.

Sandegren, L., and Andersson, D.I. (2009). Bacterial gene amplification: implications for the evolution of antibiotic resistance. *Nature Reviews Microbiology* 7, 578-588.

Sangurdekar, D.P., Zhang, Z., and Khodursky, A.B. (2011). The association of DNA damage response and nucleotide level modulation with the antibacterial mechanism of the anti-folate drug trimethoprim. *BMC genomics* 12, 583.

Schweitzer, B.I., Dicker, A.P., and Bertino, J.R. (1990). Dihydrofolate reductase as a therapeutic target. *Faseb Journal* 4, 2441-2452.

Seifert, and E. (2014). OriginPro 9.1: Scientific Data Analysis and Graphing Software—Software Review. *Journal of Chemical Information & Modeling* 54, 1552-1552.

Singer, S., Ferone, R., Walton, L., and Elwell, L. (1985). Isolation of a dihydrofolate reductase-deficient mutant of *Escherichia coli*. *Journal of bacteriology* 164, 470-472.

Spoel, D.V.D., Lindahl, E., Hess, B., Groenhof, G., and Berendsen, H.J.C. (2005). GROMACS: fast, flexible, and free. *Journal of Computational Chemistry* 26, 1701-1718.

Srinivasan, B., and Skolnick, J. (2015). Insights into the slow - onset tight - binding inhibition of *Escherichiacoli* dihydrofolate reductase: detailed mechanistic characterization of pyrrolo[3,2 - f]quinazoline - 1,3 - diamine and its derivatives as novel tight - binding inhibitors. *Febs Journal* 282, 1922-1938.

Steffan, R., and Kuhlen, T. (2001). MAESTRO: a tool for interactive assembly simulation in virtual environments. Paper presented at: Eurographics Conference on Virtual Environments & Immersive Projection Technology.

Tamer, Y.T., Gaszek, I.K., Abdizadeh, H., Batur, T.A., Reynolds, K.A., Atilgan, A.R., Atilgan, C., and Toprak, E. (2019). High-Order Epistasis in Catalytic Power of Dihydrofolate Reductase Gives Rise to a Rugged Fitness Landscape in the Presence of Trimethoprim Selection. *Molecular Biology and Evolution* *36*, 1533-1550.

Tian, J., Woodard, J.C., Whitney, A., and Shakhnovich, E.I. (2015). Thermal stabilization of dihydrofolate reductase using monte carlo unfolding simulations and its functional consequences. *PLoS Comput Biol* *11*, e1004207.

Toprak, E., Veres, A., Michel, J.-B., Chait, R., Hartl, D.L., and Kishony, R. (2012). Evolutionary paths to antibiotic resistance under dynamically sustained drug selection. *Nature genetics* *44*, 101-105.

Vestergaard, M., Paulander, W., Marvig, R.L., Clasen, J., Jochumsen, N., Molin, S., Jelsbak, L., Ingmer, H., and Folkesson, A. (2016). Antibiotic combination therapy can select for broad-spectrum multidrug resistance in *Pseudomonas aeruginosa*. *International journal of antimicrobial agents* *47*, 48-55.

Wang, J., Wang, W., Kollman, P.A., and Case, D.A. (2006). Automatic atom type and bond type perception in molecular mechanical calculations. *Journal of Molecular Graphics & Modelling* *25*, 247-260.

Warr, W.A. (2012). Scientific workflow systems: Pipeline Pilot and KNIME. *Journal of Computer Aided Molecular Design* *26*, 801-804.

Yeggoni, D.P., Gokara, M., Mark Manidhar, D., Rachamalla, A., Nakka, S., Reddy, C.S., and Subramanyam, R. (2014). Binding and Molecular Dynamics Studies of 7-Hydroxycoumarin Derivatives with Human Serum Albumin and Its Pharmacological Importance. *Molecular Pharmaceutics* *11*, 1117-1131.

Zaritsky, A., Woldringh, C.L., Einav, M., and Alexeeva, S. (2006). Use of thymine limitation and thymine starvation to study bacterial physiology and cytology. *Journal of bacteriology* *188*, 1667-1679.

Zhang, Y., Chen, Y., Zhang, D., Wang, L., Lu, T., and Jiao, Y. (2017). Discovery of Novel Potent VEGFR-2 Inhibitors Exerting Significant Antiproliferative Activity against Cancer Cell Lines. *Journal of Medicinal Chemistry* *61*, 140-157.

Zhang, Y., Chen, Y., Zhang, D., Wang, L., Lu, T., and Jiao, Y. (2018). Discovery of Novel Potent VEGFR-2 Inhibitors Exerting Significant Antiproliferative Activity against Cancer Cell Lines. *J Med Chem* *61*, 140-157.

Zhang, Y., Jiao, Y., Xiong, X., Liu, H., Ran, T., Xu, J., Lu, S., Xu, A., Pan, J., Qiao, X., *et al.* (2015). Fragment virtual screening based on Bayesian categorization for discovering novel VEGFR-2 scaffolds. *Molecular diversity* *19*, 895-913.

Zhang, Y., Yang, S., Jiao, Y., Liu, H., Yuan, H., Lu, S., Ran, T., Yao, S., Ke, Z., and Xu, J. An Integrated Virtual Screening Approach for VEGFR-2 Inhibitors. *Journal of Chemical Information & Modeling* *53*, 3163-3177.

Zhang, Y., Yang, S., Jiao, Y., Liu, H., Yuan, H., Lu, S., Ran, T., Yao, S., Ke, Z., and Xu, J. (2013). An Integrated Virtual Screening Approach for VEGFR-2 Inhibitors. *Journal of Chemical Information & Modeling* *53*, 3163-3177.

# Supplementary Information

## *Crystal structure selection.*

Through visual inspection of M20 loop conformation for the 61 crystal structures of DHFR (before 2016-9-26), crystal structures of three categories of M20 loops were obtained. From Figure S1, a total of 38 closed, 11 open, 12 occluded crystal structures of *E. coli* DHFR as well as the comparison of them are shown. The NADPH/NADP<sup>+</sup> as well as the substrates (most of them are MTX) are also shown. It can be seen that M20 loop constitutes part of the substrate binding site, so it will influence the binding of the substrates and its inhibitors. It has shown that the closed conformation is adopted when the substrate and cofactor are both bound (Agarwal et al., 2002), where the M20 loop is packed against the nicotinamide ring of the cofactor. This is the only conformation where substrate and cofactor are arranged favorably for reaction and the following state of the catalytic cycle (Agarwal et al., 2002) and also the only conformation that can be found in DHFR from all other species, regardless of the crystal packing and ligands bound positions in the binding site (Sawaya and Kraut, 1997). Observed in the product complexes, the occluded M20 loop is an unproductive conformation in which the central part of the M20 loop forms a helix that blocks access to the binding site for the nicotinamide moiety of the cofactor. Thus, the nicotinamide of the cofactor is forced out into solvent, making it unresolved in the crystal structures (Sawaya and Kraut, 1997). The open loop is a conformational intermediate between the extremes of the closed and occluded loops. The M20 loop dynamics plays a significant role in ligand binding and catalysis. It has become an area of great interest due to the persuasive evidence of conformational change in the loop during the catalytic cycle and its interaction with the substrate and cofactor (Sawaya and Kraut, 1997).

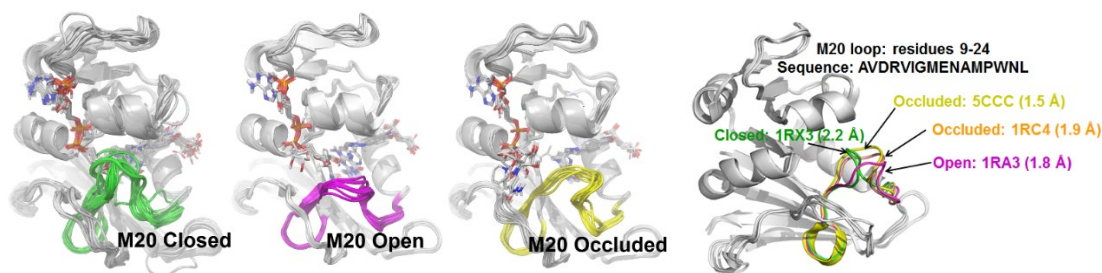


**Figure S1** Three different types of M20 loops in *E. coli* DHFR. In the crystal structures of *E. coli* DHFR, the M20 loop (residues 9-24) has three major types of conformation (open, closed and occluded) (Falzone et al.) that are important for catalysis.

However, it is still unknown which M20 loop conformation is a binding mode for inhibitors of *E. coli* DHFR. Whether binding single conformation or multiple conformations of the M20 loop leads to stronger binding is also not known. Thus, it is important to determine the target crystal structures that is most predictive for virtual screening investigation. Considering the conformation M20 loop, crystal structure resolution, as well as completeness of cognate ligands such as MTX or DDF and NADPH,

we selected four M20 loop conformations (Closed: 1RX3, Open: 1RA3, Occluded: 1RC4 and 5CCC, Figure S1) for the docking verification. Two occluded PDBs were selected because their M20 loop conformations did not overlap well. The feasibility of each M20 loop conformation was assessed by docking the known 183 *E. coli* DHFR inhibitors with IC<sub>50</sub> values ranging from 1 nM to 100 μM to the four representative PDB structures. As shown in Figure S2 and Table S1, for docking score less than -10, the cumulative numbers of selected inhibitors were 22 for the closed M20 1RX3 – greater than for the open M20 1RA3 (10), and occluded M20 1RC4 (1) and 5CCC (13). In particular, when the cutoff of docking score was set to -9, using closed M20 1RX3 as target resulted in correct prediction of as many as 62 inhibitors compared to the open M20 1RA3 (25), and occluded M20 1RC4 (4) and 5CCC (32). At the higher cutoffs, open M20 1RA3 and occluded M20 5CCC showed comparable trends with that of closed M20 1RX3. However, even the M20 loop of 1RC4 and 5CCC both belong to the occluded conformation, their performance in docking of known ligands was strikingly different. It appears that 1RC4 performed much worse than 5CCC and it performed the worst compared to other target conformations. A possible reason could be that M20 loop in 1RC4 structure is closer to the substrate, making the binding pocket smaller to accommodate relatively large inhibitors. Further, we focused on the inhibitors with IC<sub>50</sub> values less than 1 μM. As seen from Figure S2 and Figure S3, using the closed M20 1RX3 predicted about 58% (42) out of the total of 72 the inhibitors, while the open M20 1RA3 only predicted 18% (13), the occluded 1RC4 got 3% (2) and the occluded 5CCC predicted about 18% (13). Altogether these results demonstrate that the closed M20 1RX3 is more representative as a target for molecular docking of *E. coli* DHFR inhibitors.

Table S1 Number of known inhibitors by DHFR of different M20 loops

XP Docking Score Threshold	All inhibitors (IC <sub>50</sub> : 1 nM~240 μM)				Inhibitors (IC <sub>50</sub> < 1μM)			
	Closed (1RX3)	Open (1RA3)	Occluded (1RC4)	Occluded (5CCC)	Closed (1RX3)	Open (1RA3)	Occluded (1RC4)	Occluded (5CCC)
< -10	22	10	1	13	14	4	0	4
< -9	62	25	4	32	42	13	2	13
< -8	77	77	12	73	48	50	4	35
< -7	107	93	21	114	51	53	8	51
< -6	148	136	53	167	58	58	22	68
< -5	174	168	148	181	69	67	53	72
< -4	181	182	182	183	72	72	71	72
< 0	183	183	183	183	72	72	72	72



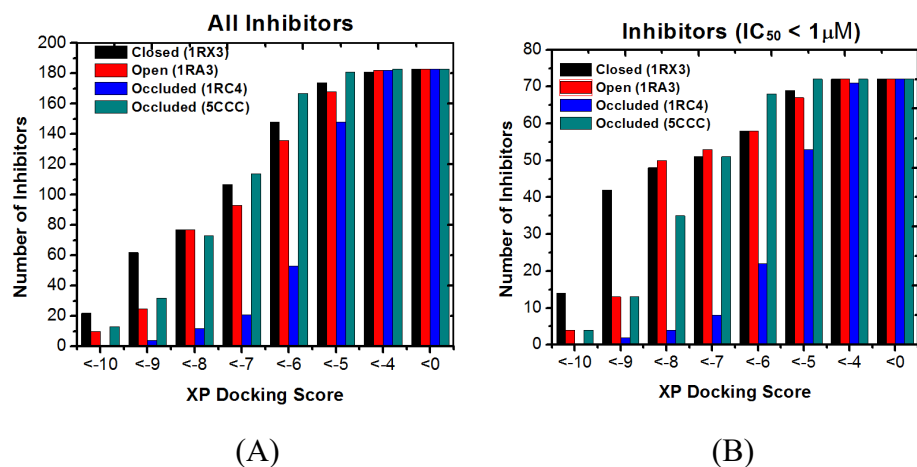


**Figure S2.** The number distribution of inhibitors with a given XP docking score. (A) All 183 inhibitors; (B) 72 Inhibitors with  $IC_{50}$  values less than  $1 \mu M$ . Lower scores correspond to stronger binding.

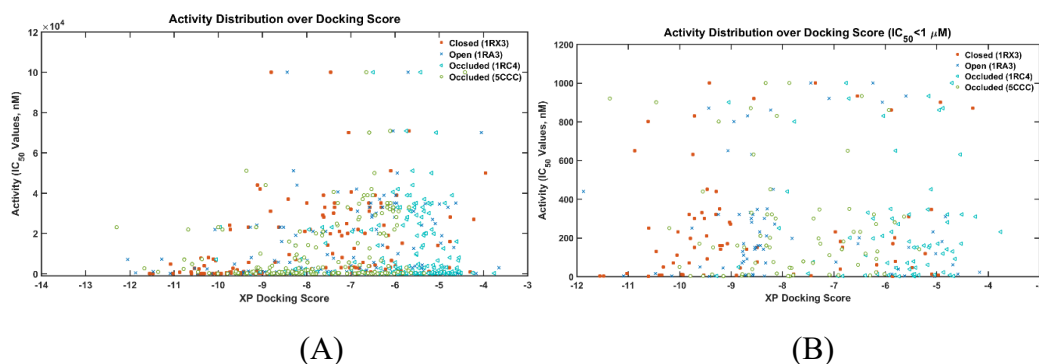


**Figure S3.** The scatter plot experimentally measured activities of DHFR inhibitors vs their XP docking score with various DHFR conformations as targets. (A) All 183 inhibitors; (B) 72 Inhibitors with  $IC_{50}$  values less than  $1 \mu M$ .

### Construction of the Model to Predict Binding Affinity.

Earlier, the MD simulation of protein-ligand complexes followed by MM/PBSA assessment of binding affinity were applied in our group to the BACE protease (Cheron and Shakhnovich, 2017). Here, we use a similar protocol for *E. coli* DHFR. Eight known *E. coli* DHFR inhibitors (Figure S4) including MTX and TMP as well as other six compounds from Carroll et al (Carroll et al., 2012) with known  $K_d$  values were chosen for the construction of binding free energy prediction. The Pearson correlation coefficient (R) between the predicted and experimental binding free energies ( $\Delta G = RT \ln(K_d)$ , where R is the gas constant and  $T = 293.15$  K) was used to evaluate the accuracy of the protocol developed in (Cheron and Shakhnovich, 2017). TMP and Cmpd 2 as well as Cmpd 6 (Figure S4) do not have crystal structures, their complexes were from molecular docking

(TMP was docked to PDB 1RX3 and Cmpd 2 and 6 were docked to 3QYL). We used the available crystal structures of TMP complexed with *Staphylococcus aureus* DHFR (PDB: 2W9G, sequence identity with *E. coli* DHFR: 55/162 (34.0%) and sequence similarity: 92/162 (56.8%)) as a reference and found that the conformation of TMP docked with *E. coli* DHFR is only about 0.4 Å different from crystal structure with *S. aureus* DHFR (Figure S5), suggesting the accuracy of docked conformation for TMP. We first conducted 2 replicates of 10 ns simulation and then extended simulation length to 20 replicates. Two replicates of 10 ns simulation provided a quite strong correlation ( $R = 0.942$ ) between the computational and experimental binding free energies (Fig.6) essentially indistinguishable from longer simulation comprised of 20 10 ns runs (Figure S6). Thus, in subsequent simulations a protocol consisting of two replicates of 10 ns was adopted. It can also be observed that the binding free energies followed a normal distribution (Figure S6) in both the short and long simulations, which indicates that the use of mean value to represent the general binding free energy is reasonable.

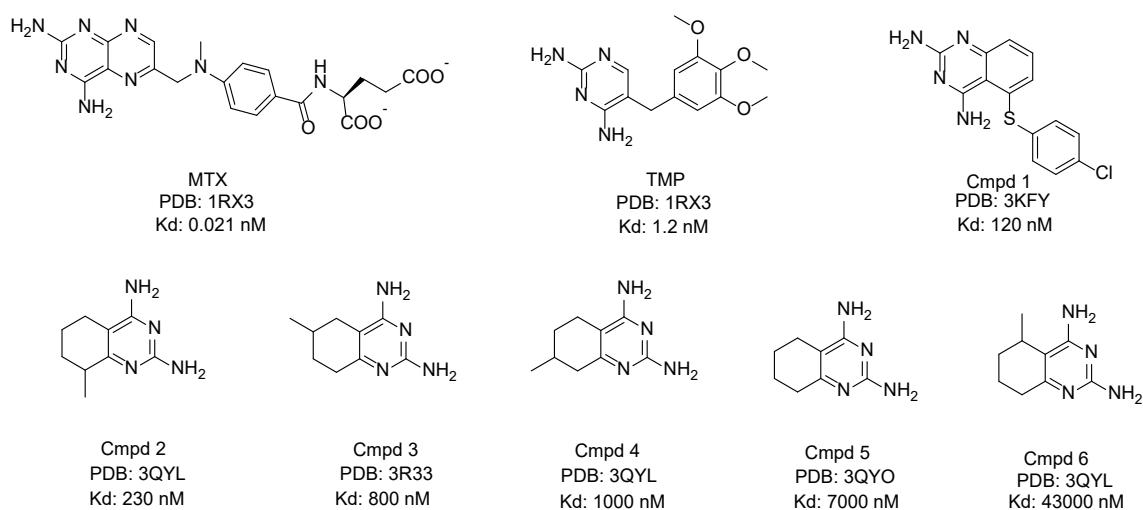


**Figure S4** Compounds used for building the binding affinity prediction model

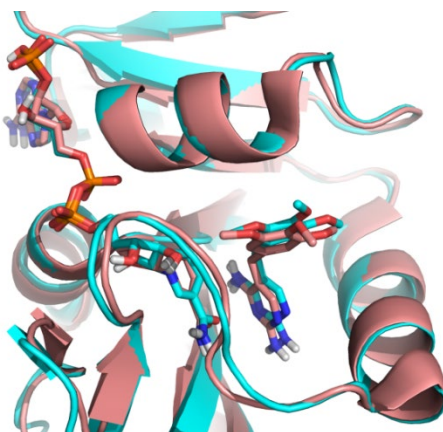


**Figure S5** Comparison of docked TMP in *E. coli* DHFR (cyan, PDB 1RX3) with crystalized TMP with *Staphylococcus aureus* DHFR (salmon, PDB: 2W9G).

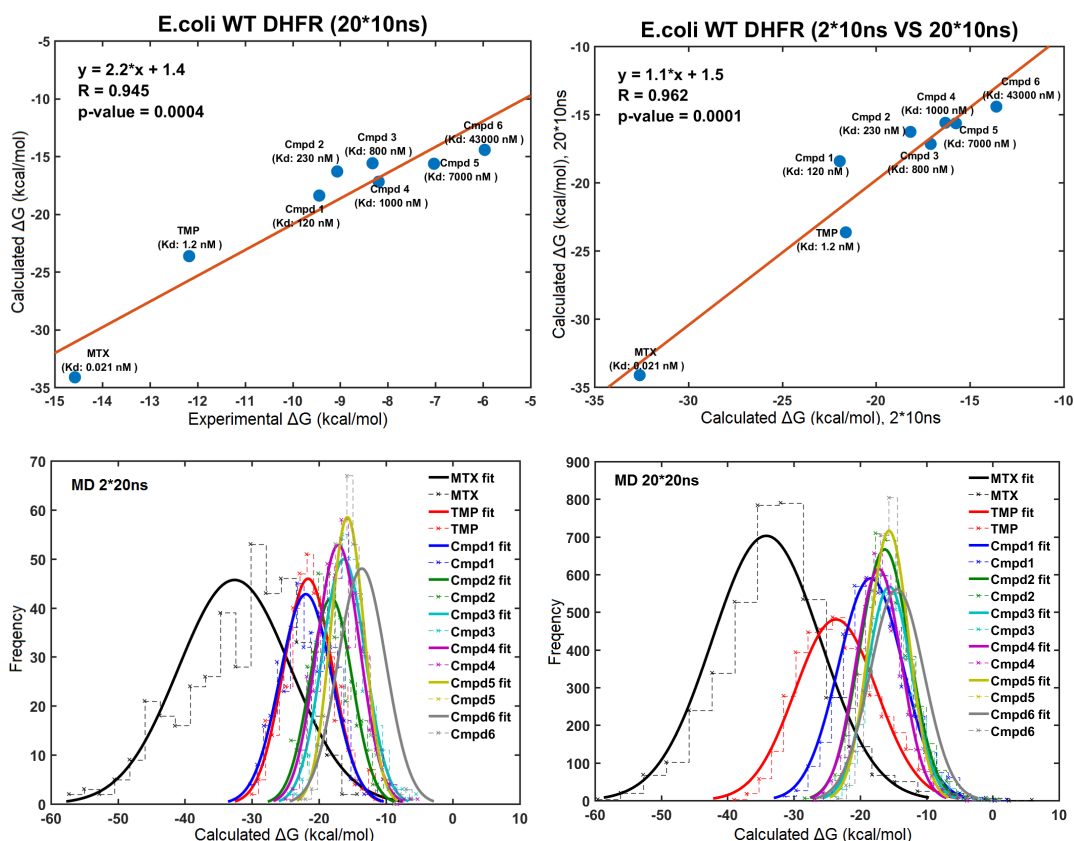


**Figure S6** Linear correlation between the computational and experimental binding Gibbs free energies for eight compounds against WT *E. coli* DHFR (upper panel). Normal distribution of binding free energies (lower panel).

An evolutionary study (Oz et al., 2014; Toprak et al., 2012) of TMP resistance found that three key resistance mutations P21L, A26T, L28R, and their combinations constitute a set that recurrently occurred in two out of five independent evolution experiments, and their order of fixation in both cases was similar. They are located within the binding pocket of dihydrofolate substrate within a small region of eight residues in the DHFR protein that constitutes a flexible Met-20 loop (residues 9–24) and an  $\alpha$ -helix (residues 25–35). Thus, the correlation coefficient between the computational and experimental binding free energies for TMP for the three mutants as well as their double and triple combinations were calculated. In addition, linear regression equation models to predict binding free energy for TMP against mutant DHFR originated from *Listeria grayi* and *Chlamydia muridarum* were also included. As shown in Figure S7, from two replicates of 10 ns simulation, the correlation coefficient (R) for *L. grayi* and *C. muridarum* DHFR were 0.895 and 0.839, respectively. The reason why the prediction for *L. grayi* and *C. muridarum* is somewhat inferior to *E. coli* DHFR ( $R=0.953$  from Figure 1C in the manuscript) may be that the protein-ligand complexes used for MD simulation are derived from molecular modeling rather than from crystal structures. Still, the values of binding free energy follow a normal distribution. Those models were used for scoring of virtual screening hits later.

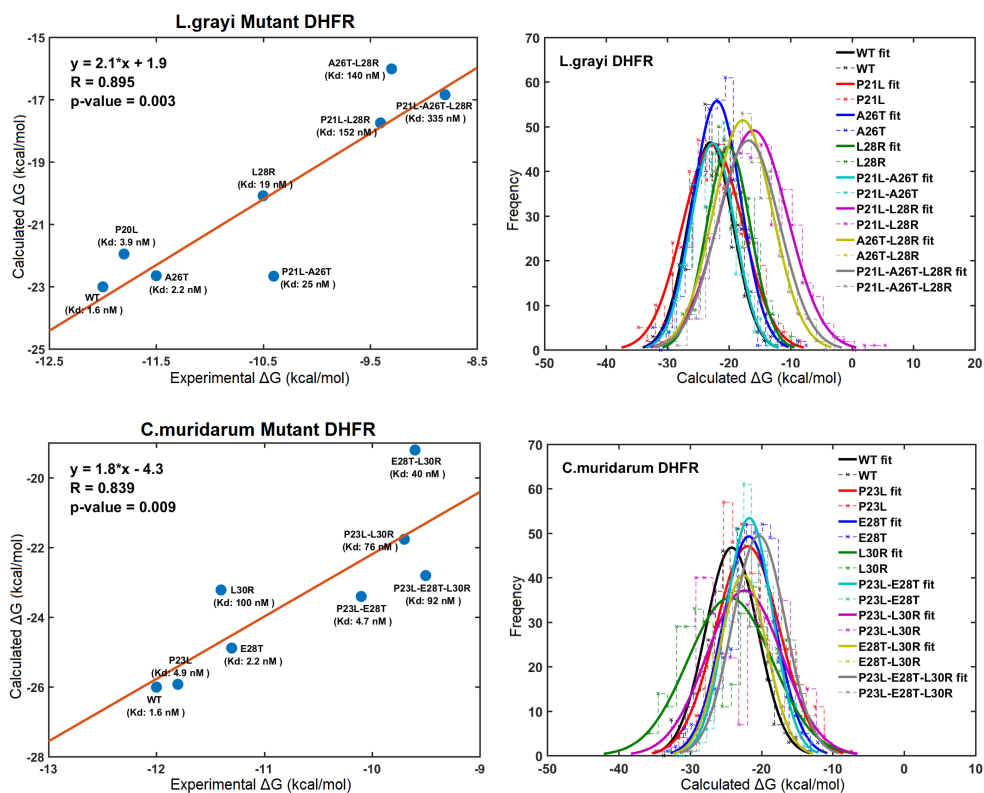


**Figure S7** Correlation and linear models for the calculated and experimental binding Gibbs free energies for TMP against WT and mutant *Listeria grayi* (upper panel) and *Chlamydia muridarum* DHFR (lower panel). Normal distribution of binding free energies (right panel).

### Selection of virtual screening hits

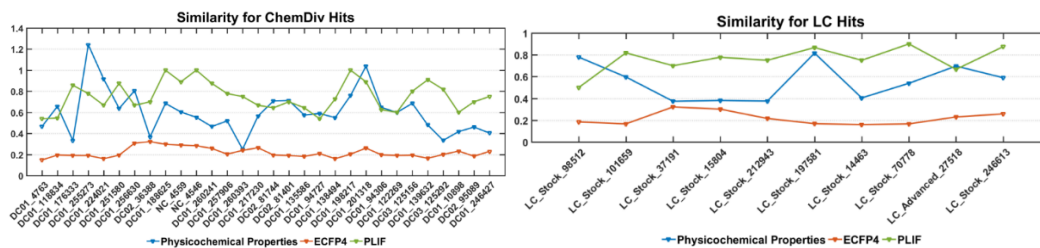
Structure-based virtual screening (SBVS) can quickly select compounds with reasonable binding patterns and higher predicted scores from a large number of compounds. According to the workflow (Figure 1A in the manuscript), a total of about 1.8 million compounds from ChemDiv and Life Chemicals were screened for compliance with the Lipinski's rule of five (Manto et al., 2018), resulting in about 1.5 million compounds. Then, a virtual screening process with three steps of different speed and precision including high throughput virtual screening (HTVS), standard precision (SP) and extra precision (XP) were respectively applied to the 1.5 million compounds. By setting different cutoff values for the HTVS of -5, SP of -7 and XP of -5, about 2900 compounds were obtained. The protein-ligand interaction of the crystal structures showed that Asp27 within the binding pocket is one of the most critical for forming hydrogen bond with known inhibitors. A total of 491 hits having contacts with Asp27 were filtered. After visual selection, 307 out of 491 compounds were submitted for the molecular dynamics evaluation using the previously selected DHFR crystal structure PDB 1RX3 as a target. Using the protocol described above we predicted the binding affinities of all 307 compounds. With a cutoff value of less than -20kcal/mol, 40 compounds were chosen for further analysis. For those 40 compounds with 32 from the ChemDiv database and 8 from the life chemicals

database we calculated their binding affinity for the WT and three single, three double and one triple mutants based on P21L, A26T and L28R. Calculations predicted significant binding affinity for all compounds not only to the wild type DHFR, but also to the DHFR mutants.

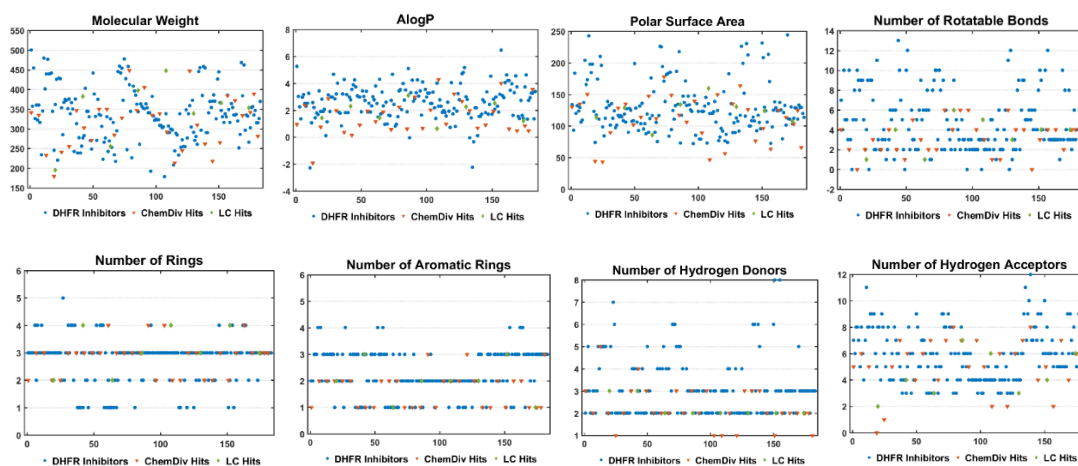
Based on the principle that compounds with similar properties tend to have similar activity (Kumar, 2011), and to ensure that the selected compounds with chemical novelty, three types of compound similarity based on Tanimoto coefficient (Zhang et al., 2013) were compared between the selected hits with that of the known 183 DHFR inhibitors. The Tanimoto coefficient uses the ratio of the intersecting set to the union set as the measure of similarity when each attribute is expressed in binary. Represented as a mathematical equation:

$$T_{AB} = \frac{c}{a + b - c}$$

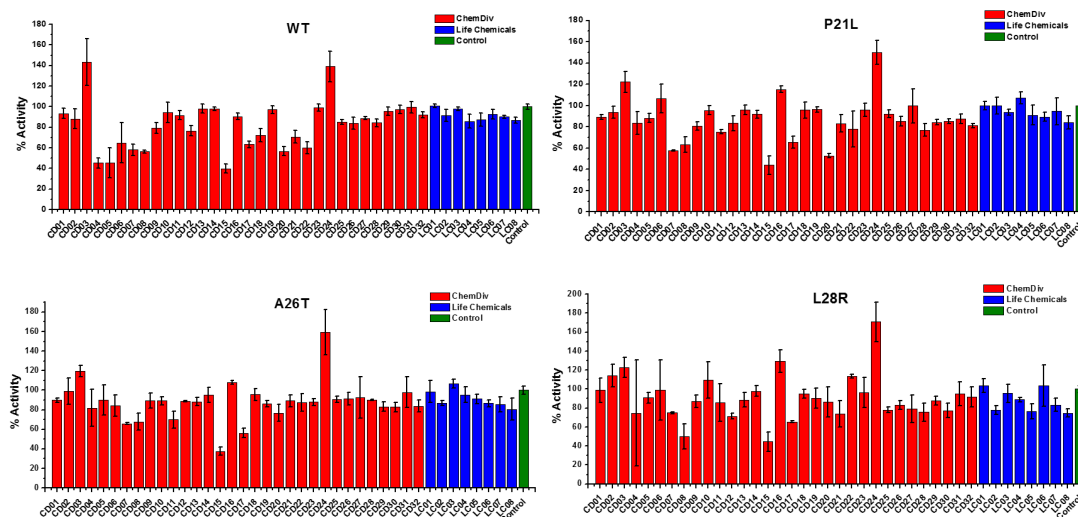
In this equation, individual fingerprint bits set in molecules A and B are represented by a and b, respectively; and c is the intersection set.  $T_{AB}$  value ranges from 0 to 1, where 0 represents that no same bits are detected; however, 1 does not mean that the two molecules are totally identical. Two-dimensional (2D) physicochemical properties including molecular weight, AlogP, polar surface area, number of rotatable bonds, rings, aromatic rings, hydrogen acceptors and hydrogen donors were compared from the two-dimensional property's aspect. Interaction similarity based on protein-ligand interaction (Huovinen et al., 1995) were calculated to ensure that the selected compounds form similar interactions with the critical binding site pocket residues which can further guarantee their biological activity. ECFP4 (Zhang et al., 2013), an extended connectivity fingerprints which can represent the chemical diversity of compounds, was used to ensure the wide chemical space and novelty in their structures. As shown in Figure S8, the 2D physicochemical properties similarity were concentrated in the range of 0.6 to 0.8 and the protein-ligand interaction fingerprint (PLIF) similarities were mainly distributed in the range of 0.7 to 0.9 on the one hand, and the ECFP4 chemical similarities were only just between 0.2 to 0.3 on the other hand. This indicated that the selected hits were of similar 2D physicochemical property and protein-ligand binding interaction but also possessed chemical diversity compared with the known DHFR inhibitors. For detailed analysis of the 2D properties for the selected hits, the predicted values above mentioned properties including molecular weight, AlogP, polar surface area, number of rotatable bonds, rings, aromatic rings, hydrogen acceptors and hydrogen donors were compared with that of the known DHFR inhibitors. It can be clearly seen from Figure S9 that those 2D properties showed similar distributions with the positive controls, further proving the effectiveness of the selected hits. Finally, selected 40 hit compounds were submitted for purchase and biological activity evaluation.



**Figure S8** Similarity comparison between the selected hits with the known inhibitors using physicochemical properties, structure (represented by ECFP4) and PLIF.



**Figure S9** Two-dimensional chemical space of physicochemical properties for the selected hits with the known DHFR inhibitors.



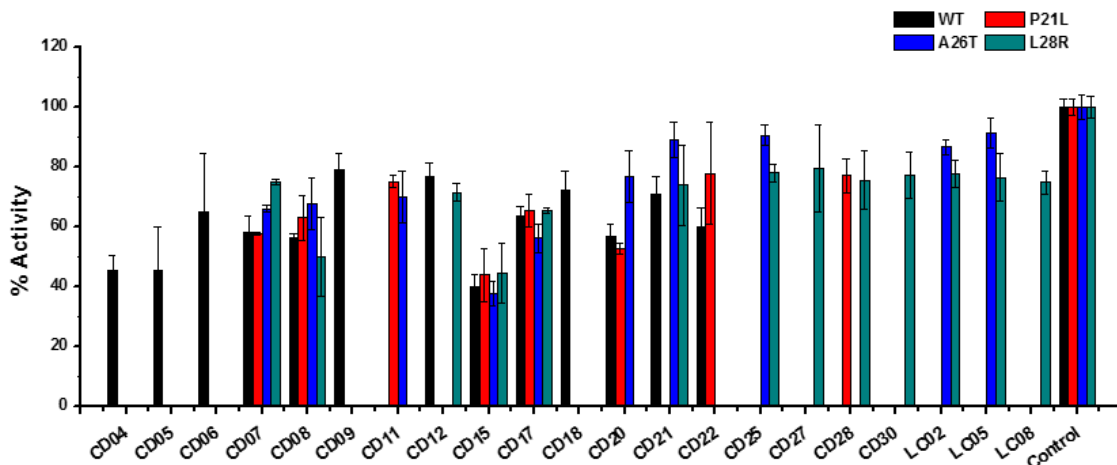


**Figure S10** The initial inhibition rate of catalytic activity of the selected 40 hits against WT and three DHFR mutants at a single concentration of 200 μM. Each experiment was conducted in triplicates.

**Table S2** The  $K_i$  values (in μM) for compounds CD15 and CD17.

Species	DHFR Type	CD15		CD17	
		Ki Value	STD <sup>a</sup>	Ki Value	STD
<i>E. coli</i>	WT	3.35	0.28	8.18	0.29
	P21L	1.42	0.04	3.7	0.13
	A26T	2.43	0.37	6.73	1.02
	L28R	1.04	0.07	3.65	0.33
	P21L-A26T	3.26	0.21	9.2	0.71
	P21L-L28R	0.56	0.05	1.37	0.06
	A26T-L28R	0.61	0.04	2.04	0.11
<i>L. grayi</i>	WT	5.01	0.29	16.17	1.7
<i>C. muridarum</i>	WT	14.6	0.64	32.38	2.53
Human	WT	0.38	0.05	0.74	0.1

<sup>a</sup>STD means the standard error from three duplicate experiments.



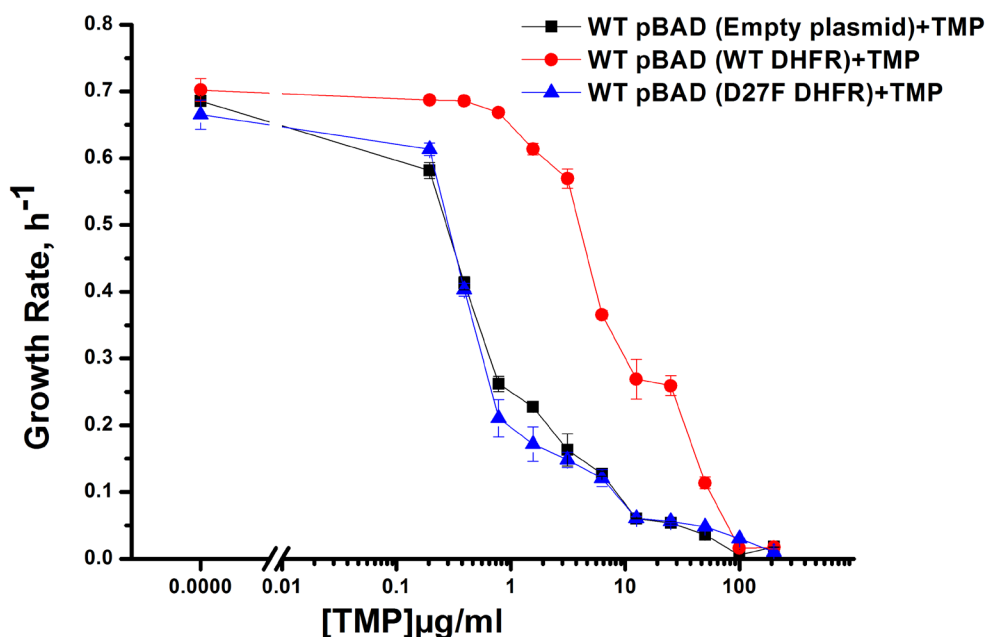


**Figure S11:** Growth rate profiles of WT *E. coli* cells with empty pBAD-plasmid and with WT DHFR and functionally inactive D27F mutant form of DHFR. Expression was induced using 0.005% Arabinose and cells were grown in M9 media. Plot shows overexpression of functional form of DHFR i.e. WT DHFR can recover the growth rates of cells growing in presence of TMP. Overexpression of D27F failed to recover growth rates of TMP treated cells.

## References

- Agarwal, P.K., Billeter, S.R., Rajagopalan, P.T., Benkovic, S.J., and Hammes-Schiffer, S. (2002). Network of coupled promoting motions in enzyme catalysis. *Proc Natl Acad Sci U S A* 99, 2794-2799.
- Carroll, M.J., Mauldin, R.V., Gromova, A.V., Singleton, S.F., Collins, E.J., and Lee, A.L. (2012). Evidence for dynamics in proteins as a mechanism for ligand dissociation. *Nature chemical biology* 8, 246-252.
- Cheron, N., and Shakhnovich, E.I. (2017). Effect of sampling on BACE-1 ligands binding free energy predictions via MM-PBSA calculations. *J Comput Chem* 38, 1941-1951.
- Falzone, C.J., Wright, P.E., and Benkovic, S.J. Dynamics of a flexible loop in dihydrofolate reductase from *Escherichia coli* and its implication for catalysis. *Biochemistry* 33, 439-442.
- Huovinen, P., Sundström, L., Swedberg, G., and Sköld, O. (1995). Minireview. Trimethoprim and sulfonamide resistance. *Antimicrobial Agents & Chemotherapy* 39, 279-289.
- Kumar, A. (2011). Investigation of structures similarity of organic substances. *Resonance* 16, 61-64.



Manto, C.C., Sara, M., and Laleh, A. (2018). Drug Metabolites and their Effects on the Development of Adverse Reactions: Revisiting Lipinski's Rule of Five. *International Journal of Pharmaceutics* 549, 133-149.

Oz, T., Guvenek, A., Yildiz, S., Karaboga, E., Tamer, Y.T., Mumcuyan, N., Ozan, V.B., Senturk, G.H., Cokol, M., Yeh, P., *et al.* (2014). Strength of selection pressure is an important parameter contributing to the complexity of antibiotic resistance evolution. *Mol Biol Evol* 31, 2387-2401.

Sawaya, M.R., and Kraut, J. (1997). Loop and subdomain movements in the mechanism of Escherichia coli dihydrofolate reductase: crystallographic evidence. 36, 586.

Toprak, E., Veres, A., Michel, J.-B., Chait, R., Hartl, D.L., and Kishony, R. (2012). Evolutionary paths to antibiotic resistance under dynamically sustained drug selection. *Nature genetics* 44, 101-105.

Zhang, Y., Yang, S., Jiao, Y., Liu, H., Yuan, H., Lu, S., Ran, T., Yao, S., Ke, Z., and Xu, J. An Integrated Virtual Screening Approach for VEGFR-2 Inhibitors. *Journal of Chemical Information & Modeling* 53, 3163-3177.

Zhang, Y., Yang, S., Jiao, Y., Liu, H., Yuan, H., Lu, S., Ran, T., Yao, S., Ke, Z., and Xu, J. (2013). An Integrated Virtual Screening Approach for VEGFR-2 Inhibitors. *Journal of Chemical Information & Modeling* 53, 3163-3177.

<b>Compound ID</b>	<b>Source Database</b>	<b>Compound Code (ChemDiv)</b>	<b>Docking Score</b>
CD01	ChemDiv	4361-0444	-6.969
CD02	ChemDiv	6773-1654	-9.195
CD03	ChemDiv	8019-6404	-7.433
CD04	ChemDiv	8011-5588	-9.354
CD05	ChemDiv	8019-8601	-8.003
CD06	ChemDiv	D043-0124	-6.264
CD07	ChemDiv	7999-4501	-5.317
CD08	ChemDiv	7999-4516	-7.295
CD09	ChemDiv	7999-4493	-5.343
CD10	ChemDiv	8020-4876	-6.782
CD11	ChemDiv	8020-0785	-6.778
CD12	ChemDiv	8020-5139	-7.117
CD13	ChemDiv	8009-3393	-6.826
CD14	ChemDiv	D364-1686	-5.992
CD15	ChemDiv	D364-0564	-5.502
CD16	ChemDiv	4891-2123	-6.856
CD17	ChemDiv	3739-0010	-6.906
CD18	ChemDiv	5042-0801	-6.756
CD19	ChemDiv	8004-4149	-6.742
CD20	ChemDiv	8005-2585	-6.42
CD21	ChemDiv	3729-2217	-6.569
CD22	ChemDiv	4449-1085	-5.952
CD23	ChemDiv	1016-0032	-6.26
CD24	ChemDiv	5107-0106	-6.416
CD25	ChemDiv	4965-0168	-5.443
CD26	ChemDiv	0929-0063	-5.397
CD27	ChemDiv	D451-1524	-5.835
CD28	ChemDiv	8017-8695	-5.127
CD29	ChemDiv	8011-1945	-7.227
CD30	ChemDiv	7706-1220	-7.933
CD31	ChemDiv	D364-1754	-5.767
CD32	ChemDiv	F2209-0009	-7.011

<b>Compound ID</b>	<b>Source Database</b>	<b>Compound Code (Life Chemicals)</b>	<b>docking score</b>
LC01	Life Chemicals	F9995-0268	-8.157
LC02	Life Chemicals	F6497-6796	-6.351
LC03	Life Chemicals	F1967-0017	-5.632
LC04	Life Chemicals	F3184-0059	-6.377
LC05	Life Chemicals	F6497-5769	-6.856
LC06	Life Chemicals	F6497-5836	-7.509
LC07	Life Chemicals	F6497-5805	-6.604
LC08	Life Chemicals	F1765-0082	-7.538

<b>Compound ID</b>	<b>SourceName</b>	<b>Compound code (ChemDiv)</b>	<b>docking score</b>
CD15	ChemDiv	D364-0564	-6.26
CD15-1	ChemDiv	D364-0563	-6.09
CD15-2	ChemDiv	D364-0577	-6.60
CD15-3	ChemDiv	D364-0578	-6.03
CD15-4	ChemDiv	D364-0576	-5.69
CD15-5	ChemDiv	8012-9116	-5.80
CD15-6	ChemDiv	D364-0566	-6.15
CD17	ChemDiv	3739-0010	-7.04
CD17-1	ChemDiv	2817-0146	-7.87
CD17-2	ChemDiv	2897-1527	-7.58
CD17-3	ChemDiv	3699-1145	-7.37
CD17-4	ChemDiv	2897-0417	-7.60
CD17-5	ChemDiv	8008-9070	-7.09
CD17-6	ChemDiv	2817-0079	-7.40

### Hits Information

Glide RMSD(XP to S	Calculated $\Delta G$ for WT	Molecular_Wei	Num_H_Donor	Num_H_Accept
0.449	-31.54340	341.114	3	5
0.161	-28.83145	334.395	2	6
0.003	-26.86650	232.199	5	5
0.414	-26.69280	179.214	2	0
0.338	-21.62680	241.209	1	1
0.104	-21.00510	255.275	2	5
0.032	-36.12370	346.338	3	7
0.843	-26.73540	302.285	4	6
0	-20.00060	270.287	3	4
0.142	-30.08950	349.405	2	6
0.458	-30.05510	349.362	2	7
0.066	-27.22290	284.336	2	4
0.015	-24.14395	327.252	3	7
0.262	-36.28520	448.493	2	8
0.061	-33.75800	346.338	3	7
0.471	-24.58235	405.403	2	5
0.01	-20.23215	334.281	3	7
0.938	-26.80810	338.357	1	5
0.397	-21.79460	292.16	1	2
0.001	-21.34925	213.283	2	6
0.004	-20.56175	244.676	1	2
0.153	-28.08425	447.236	3	6
0.55	-22.55530	309.298	3	7
0.588	-21.23050	261.237	3	8
0.175	-20.85190	218.255	2	4
0.431	-20.18265	265.285	1	5
0.048	-27.34900	383.871	2	2
0.45	-20.82425	371.347	2	7
0.78	-20.92805	333.342	2	4
0.92	-20.27730	342.346	2	6
0.20	-34.85515	388.375	2	7
3.378	-22.16185	281.306	1	3

glide rmsd(XP to SP)	$\Delta G$ for WT	MD	Molecular_Wei	Num_H_Donor	Num_H_Accept
0.007	-29.21460	195.22	3	3	2
0.056	-27.10690	382.39	3	3	4
0.056	-20.55160	255.63	2	2	3
6.596	-20.30705	397.45	2	2	7
0.963	-26.84855	447.51	2	2	6
0.178	-21.07285	338.81	2	2	3
0.19	-20.90360	365.39	2	2	4
0.439	-30.32630	353.37	2	2	6

<b>glide rmsd to input</b>	<b>MD <math>\Delta G</math> for WT</b>	<b>Molecular_Wei</b>	<b>Num_H_Donor</b>	<b>Num_H_Accept</b>
0.0005	-33.75850	346.34	3	7
0.0005	-31.20530	330.34	3	6
0.0005	-33.23110	332.31	4	7
0.0005	-32.09240	336.35	3	5
0.0005	-28.01960	330.30	3	7
0.0005	-25.36605	289.25	4	6
0.0006	-30.66325	376.36	3	8
0.6384	-20.23215	334.28	3	7
0.2635	-21.64780	369.12	3	6
0.1211	-20.44430	320.25	3	7
0.0005	-25.89070	304.26	3	6
0.0005	-22.35690	359.12	3	6
0.0005	-21.95720	266.25	2	3
0.0005	-23.77155	445.22	3	6

<b>ALogP</b>	<b>Num_Rot</b>	<b>Num_Rin</b>	<b>Num_Aro</b>	<b>Molecular_FractionalPolar</b>	<b>ECFP4</b>	<b>Similarity with known DHF</b>
0.95	4	2	1	0.381	0.195	
2.355	2	3	2	0.403	0.191	
-1.927	0	3	2	0.647	0.19	
0.751	2	2	2	0.246	0.16	
2.869	3	2	2	0.18	0.308	
1.987	2	3	2	0.35	0.322	
0.365	4	3	1	0.371	0.297	
0.155	2	3	1	0.446	0.289	
0.9	1	3	1	0.377	0.283	
1.936	5	3	2	0.326	0.258	
1.165	3	4	2	0.421	0.203	
1.864	2	3	2	0.393	0.239	
0.556	2	3	1	0.543	0.264	
2.217	6	3	1	0.331	0.195	
0.606	4	3	1	0.339	0.19	
2.979	6	4	3	0.262	0.182	
0.661	6	2	1	0.417	0.208	
2.034	4	4	2	0.263	0.16	
4.284	3	2	2	0.159	0.203	
0.981	1	2	2	0.702	0.261	
3.198	1	3	3	0.231	0.196	
2.665	6	3	2	0.302	0.191	
1.981	4	2	1	0.529	0.193	
0.684	4	2	1	0.482	0.164	
0.918	0	3	2	0.349	0.2	
1.909	3	2	1	0.362	0.232	
3.995	4	3	2	0.165	0.184	
0.614	4	4	2	0.337	0.224	
0.475	2	3	1	0.341	0.235	
0.846	4	3	1	0.302	0.192	
0.473	4	3	1	0.321	0.182	
3.552	3	3	3	0.235	0.258	

<b>ALogP</b>	<b>Num_Rot</b>	<b>Num_Rin</b>	<b>Num_Aro</b>	<b>Molecular_FractionalPolar</b>	<b>ECFP4</b>	<b>Similarity with known DHF</b>
1.429	1	2	2	0.583	0.185	
2.288	4	4	3	0.337	0.167	
1.421	1	2	1	0.336	0.302	
3.086	6	3	2	0.337	0.216	
0.637	5	4	2	0.356	0.169	
2.245	3	3	2	0.386	0.16	
2.525	4	4	3	0.34	0.167	
1.202	4	3	1	0.304	0.23	

<b>ALogP</b>	<b>Num_Rot</b>	<b>Num_Rin</b>	<b>Num_Aro</b>	<b>Molecular_FractionalPol</b>	<b>PLIF Similarity with CD15 or CD1</b>
0.61	4	3	1	0.34	1.00
0.97	4	3	1	0.33	1.00
0.38	3	3	1	0.40	0.89
1.55	2	4	2	0.31	0.88
0.41	2	4	1	0.38	0.88
-0.94	3	2	1	0.49	0.78
0.59	5	3	1	0.33	0.50
0.66	6	2	1	0.42	1.00
1.08	4	2	1	0.41	0.93
0.31	5	2	1	0.44	0.79
0.81	4	2	1	0.43	0.63
1.66	4	2	1	0.39	0.60
1.77	1	3	2	0.31	0.50
2.81	5	3	2	0.33	0.47

**R inhibitors**

**R inhibitors**



Name	Type	Minimum	Maximum
porin CDS	CDS	571214	572281
Lysis protein S homolog from lambdoid prophage DLP12 CDS	CDS	572854	573069
lysozyme RrrD CDS	CDS	573069	573566
DLP12 prophage; murein endopeptidase CDS	CDS	573563	574024
Lipoprotein bor homolog from lambdoid prophage DLP12 CDS	CDS	574056	574349
DLP12 prophage; uncharacterized protein CDS	CDS	574640	575050
DLP12 prophage; uncharacterized protein CDS	CDS	575336	575542
DUF3950 domain-containing protein CDS	CDS	575707	575901
DNA-packaging protein CDS	CDS	576049	576150
DNA-packaging protein NU1 homolog CDS	CDS	576290	576835
tail assembly protein CDS	CDS	576810	577553
SAM-dependent methyltransferase CDS	CDS	577608	578039
phage tail protein CDS	CDS	578331	578591
transcriptional regulator CDS	CDS	579137	579886
protease 7 CDS	CDS	580136	581089
porin thermoregulatory protein EnvY CDS	CDS	581603	582364
PRK09936 family protein CDS	CDS	582547	583437
bacteriophage N4 adsorption protein A CDS	CDS	583438	586410
nfrB CDS	CDS	586397	588634
two-component sensor histidine kinase CDS	CDS	588784	590226
DNA-binding response regulator CDS	CDS	590216	590899
cation efflux system protein CusC CDS	CDS	591056	592429
cation efflux system protein CusF CDS	CDS	592587	592919
cation efflux system protein CusB CDS	CDS	592935	594158
cation efflux system protein CusA CDS	CDS	594170	597313
phenylalanine-specific permease CDS	CDS	597415	598791
miniconductance mechanosensitive channel YbdG CDS	CDS	598872	600119
NAD(P)H-dependent oxidoreductase CDS	CDS	600227	600880
DUF419 domain-containing protein CDS	CDS	600974	601342
DUF1158 domain-containing protein CDS	CDS	601407	601655
weak gamma-glutamyl:cysteine ligase CDS	CDS	601721	602839
protein HokE CDS	CDS	603292	603444
transposase CDS	CDS	603521	604633
4'-phosphopantetheinyl transferase CDS	CDS	604915	605544
ferrienterobactin receptor CDS	CDS	605710	607950
enterochelin esterase CDS	CDS	608193	609395
enterobactin biosynthesis protein YbdZ CDS	CDS	609398	609616
entF CDS	CDS	609613	613494
ferric enterobactin transporter FepE CDS	CDS	613710	614843
ferric enterobactin transport ATP-binding protein FepC CDS	CDS	614840	615655
ferric anguibactin ABC transporter permease CDS	CDS	615652	616644
ferric anguibactin ABC transporter permease CDS	CDS	616641	617645
enterobactin exporter EntS CDS	CDS	617756	619006
ferrienterobactin-binding periplasmic protein CDS	CDS	619010	619966
isochorismate synthase EntC CDS	CDS	620341	621516
entE CDS	CDS	621526	623136

enterobactin synthase component B CDS	CDS	623150	624007
2,3-dihydro-2,3-dihydroxybenzoate dehydrogenase CDS	CDS	624007	624753
proofreading thioesterase EntH CDS	CDS	624756	625169
carbon starvation protein A CDS	CDS	625350	627455
oxidoreductase CDS	CDS	627845	628933
methionine aminotransferase CDS	CDS	629042	630202
phosphoadenosine phosphosulfate reductase CDS	CDS	630805	632025
transcriptional regulator CDS	CDS	632172	633074
dsbG CDS	CDS	633283	634029
alkyl hydroperoxide reductase subunit C CDS	CDS	634401	634964
alkyl hydroperoxide reductase subunit F CDS	CDS	635209	636774
universal stress protein G CDS	CDS	636895	637323
glutathione-dependent formaldehyde dehydrogenase CDS	CDS	637544	638782
nucleoside diphosphate kinase regulator CDS	CDS	639013	639423
ribonuclease I CDS	CDS	639653	640459
anion permease CDS	CDS	640573	642036
citG CDS	CDS	642087	642965
citX CDS	CDS	642940	643491
citrate lyase alpha chain CDS	CDS	643495	645027
citrate lyase subunit beta CDS	CDS	645038	645946
citrate lyase ACP CDS	CDS	645943	646239
[citrate (pro-3S)-lyase] ligase CDS	CDS	646254	647312
dpiB CDS	CDS	647691	649349
dpiA CDS	CDS	649318	649998
dcuC CDS	CDS	650039	651424

Length	Direction	Category
1068	reverse	Transporter and Pumps
216	forward	Phage Element
498	forward	Phage Element
462	forward	Phage Element
294	reverse	Phage Element
411	reverse	Phage Element
207	forward	Phage Element
195	reverse	Phage Element
102	forward	Phage Element
546	forward	Phage Element
744	forward	Phage Element
432	reverse	Metabolic
261	forward	Phage Element
750	forward	Transcription-Translation Regulation
954	reverse	Transporter and Pumps
762	reverse	Transporter and Pumps
891	reverse	Transporter and Pumps
2973	reverse	Phage element
2238	reverse	Phage element
1443	reverse	Transporter and Pumps
684	reverse	Transporter and Pumps
1374	forward	Transporter and Pumps
333	forward	Transporter and Pumps
1224	forward	Transporter and Pumps
3144	forward	Transporter and Pumps
1377	forward	Transporter and Pumps
1248	reverse	Transporter and Pumps
654	reverse	Metabolic
369	reverse	Phage element
249	reverse	Phage element
1119	reverse	Metabolic
153	forward	Transcription-Translation Regulation
1113	forward	Transposable Element
630	reverse	Transposable Element
2241	reverse	Transporter and Pumps
1203	forward	Transporter and Pumps
219	forward	Transporter and Pumps
3882	forward	Transporter and Pumps
1134	forward	Transporter and Pumps
816	reverse	Transporter and Pumps
993	reverse	Transporter and Pumps
1005	reverse	Transporter and Pumps
1251	forward	Transporter and Pumps
957	reverse	Transporter and Pumps
1176	forward	Transporter and Pumps
1611	forward	Transporter and Pumps

858 forward	Transporter and Pumps
747 forward	Metabolic
414 forward	Metabolic
2106 forward	Metabolic
1089 reverse	Metabolic
1161 forward	Metabolic
1221 reverse	Metabolic
903 reverse	Transcription-Translation Regulation
747 reverse	Transcription-Translation Regulation
564 forward	Other (Chaperone)
1566 forward	Other (Stress Response Gene)
429 reverse	Other (Stress Response Gene)
1239 forward	Metabolic
411 reverse	Metabolic
807 reverse	Transcription-Translation Regulation
1464 reverse	Transporter and Pumps
879 reverse	Metabolic
552 reverse	Metabolic
1533 reverse	Metabolic
909 reverse	Metabolic
297 reverse	Metabolic
1059 reverse	Metabolic
1659 forward	Metabolic
681 forward	Transcription-Translation Regulation
1386 reverse	Transporter and Pumps